Title: Methyl-Metabolite Depletion Elicits Adaptive Responses to Support Heterochromatin Stability and Epigenetic Persistence

Spencer A. Haws[1,2], Deyang Yu[3,4,5], Cunqi Ye[6], Coral K. Wille[1,6], Long C. Nguyen[8,9], Kimberly A. Krautkramer[1,2,] Jay L. Tomasiewicz[3], Shany E. Yang[3,4], Blake R. Miller[3,4], Wallace H. Liu[1,2], Kazuhiko Igarashi[8,9], Rupa Sridharan[1,6], Benjamin P. Tu[6], Vincent L. Cryns[3,5,10], Dudley W. Lamming[3,4,5], and John M. Denu[1,2*].

[1]Department of Biomolecular Chemistry, SMPH, University of Wisconsin, Madison, WI, 53706, USA

[2]Wisconsin Institute for Discovery, University of Wisconsin, Madison, WI, 53715, USA

[3]Department of Medicine, SMPH, University of Wisconsin, Madison, WI, 53705, USA

[4]William S. Middleton Memorial Veterans Hospital, Madison, WI, 53705, USA

[5]Molecular & Environmental Toxicology Center, SMPH, University of Wisconsin, Madison, WI, 53705, USA

[6]Department of Biochemistry, University of Texas Southwestern Medical Center, Dallas, TX, 75390, USA

[7]Department of Cell and Regenerative Biology, University of Wisconsin, Madison, WI, 53705, USA

[8]Department of Biochemistry, Tohoku University Graduate School of Medicine, Sendai, 980-8575, JPN

[9]Center for Regulatory Epigenome and Diseases, Tohoku University Graduate School of Medicine, Sendai, 980-8575, JPN

[10]University of Wisconsin Carbone Cancer Center, Madison, WI, 53792, USA

*Correspondence: John M. Denu, john.denu@wisc.edu

Summary

S-adenosylmethionine (SAM) is the methyl-donor substrate for DNA and histone methyltransferases that regulate cellular epigenetic states. This metabolism-epigenome link enables the sensitization of chromatin methylation to altered SAM abundance. However, a chromatin-wide understanding of the adaptive/responsive mechanisms that allow cells to actively protect epigenetic information during life-experienced fluctuations in SAM availability are unknown. We identified a robust response to SAM depletion that is highlighted by preferential cytoplasmic and nuclear *de novo* mono-methylation of H3 Lys 9 (H3K9) at the expense of global losses in histone di- and tri-methylation. Under SAM-depleted conditions, *de novo* H3K9 mono-methylation preserves heterochromatin stability and supports global epigenetic persistence upon metabolic recovery. This unique chromatin response was robust across the mouse lifespan and correlated with improved metabolic health, supporting a significant role for epigenetic adaptation to SAM depletion *in vivo*. Together, these studies provide the first evidence for active epigenetic adaptation and persistence to metabolic stress.

Keywords: metabolism, methionine, SAM, epigenetics, methylation, chromatin, histone, aging, persistence

46 **Introduction**

47

48 Metabolism and the epigenome are connected by central metabolites that act as co-
49 substrates for chromatin modifying enzymes, enabling fluctuations in metabolite availability to
50 directly tune a cell's ability to 'write' and 'erase' chromatin post-translational modifications
51 (PTMs) (Fan et al., 2015; Li et al., 2018). Chromatin methylation has been shown to be
52 particularly susceptible to metabolic perturbations as methyltransferases require a single
53 methyl-donor cofactor, S-adenosylmethionine (SAM) (Ducker and Rabinowitz, 2016; Mentch
54 and Locasale, 2017). For example, accumulation of SAM in *S. cerevisiae* results in global
55 increases in histone methylation levels (Ye et al., 2017). On the contrary, reduced SAM
56 availability has been linked with site-specific losses in histone methylation as well as global
57 depression of DNA methylation in several organisms (Shiraki et al., 2014; Ding et al., 2015; Kera
58 et al., 2013; Tang et al., 2017; Shyh-Chang et al., 2013; Mentch et al., 2015; Tang et al., 2015;
59 Hayashi et al., 2018; Towbin et al., 2012; Strekalova et al., 2019; Wang et al., 2019).
60 Intracellular SAM abundance is dependent on the catalysis of its obligatory precursor
61 metabolite, the essential amino acid methionine (Met). Consumption of popular diets containing
62 low quantities of Met (fish, vegetarian, and vegan) have been shown to significantly correlate
63 with decreased plasma Met concentrations (Farmer, 2014; Schmidt et al., 2016). This link
64 provides an opportunity for diet to directly influence intracellular SAM availability. Furthermore,
65 abundance of Met and SAM have both been shown to fluctuate naturally in tune with circadian
66 rhythms (Krishnaiah et al., 2017). Therefore, individuals consuming adequate amounts of
67 dietary Met likely still experience periods of decreased methyl-metabolite availability. While
68 both dietary intake and circadian regulation are capable of influencing Met and SAM
69 abundance, adaptive mechanisms that allow cells to actively respond to – and recover their
70 functional epigenomes from – such metabolic perturbations are unknown. Here, we define the
71 ability of a cell and/or organism to re-establish the epigenome that was present prior to onset of
72 an environmental perturbation or metabolic stress as *epigenetic persistence*.
73 Adaptive mechanisms that respond to methyl-metabolite depletion likely support critical
74 cellular functions under these conditions. Interestingly, dietary Met-restriction is associated with
75 beneficial metabolic reprogramming and lifespan extension in mammals (Orentreich et al., 1993;
76 Yu et al., 2018; Miller et al., 2005; Brown-Borg et al., 2018; Lees et al., 2014; Green and
77 Lamming, 2018). These phenotypes run counter to negative pathologies associated with
78 dysregulated chromatin methylation (i.e., intellectual disability syndromes, cancers, and
79 premature as well as natural aging) (Greer and Shi, 2012). This suggests cells possess

80 responsive mechanisms capable of actively maintaining regulation of site specific and/or global
81 chromatin methylation events during SAM depletion. The goal of this study is to identify and
82 characterize such mechanisms to better understand how organisms actively protect their
83 epigenome in response to fluctuations in central metabolite availability.
84 Here, we identify a robust, conserved chromatin response to metabolically-depleted
85 SAM levels. This cellular response is characterized by global decreases in higher-state histone
86 methylation (di- and tri-methyl) and simultaneous coordinated activation of *de novo* H3K9 mono-
87 methylation involving newly-synthesized and chromatin-bound histone H3. Under extreme
88 conditions of both reduced SAM levels and inhibited methylation that would yield H3K9me1,
89 heterochromatin instability and de-repression of constitutively silenced DNA elements is
90 exacerbated. Acute inhibition of *de novo* H3K9 mono-methylation also leads to the
91 dysregulation of global histone PTM states upon metabolic recovery, disrupting epigenetic
92 persistence to decreased SAM availability. Importantly, chronic metabolic depletion of SAM in
93 both young and old mice recapitulates these *in vitro* findings, revealing a conserved, age-
94 independent chromatin response. These results implicate *de novo* H3K9 mono-methylation as
95 an indispensable mechanism to support heterochromatin stability and global epigenetic
96 persistence in response to SAM depletion.
97
98 **Results**
99
100 Methionine Restriction Stimulates Dynamic Histone PTM Response
101
102 To comprehensively investigate how disruption of methyl-donor metabolism affects
103 chromatin methylation states, global histone proteomics and DNA methylation (5mC) analyses
104 were performed on two distinct *in vitro* and *in vivo* systems. These included Met-restricted
105 HCT116 human colorectal cancer cells and C57BL/6J mouse liver. Methionine metabolism was
106 severely repressed in both systems, highlighted by significant reductions in Met and SAM
107 abundance (Figure 1A and Figure S1A-S1D). Reduced methyl-metabolite availability did not
108 affect global DNA 5mC abundance in either system (Figure 1B-1C). However, LC-MS/MS
109 analysis of more than 40 unique histone H3 peptide proteoforms revealed dynamic PTM
110 responses to Met-restriction in both HCT116 cells and C57BL/6J liver (Figure 1D-1E). In
111 HCT116 cells, Met-restriction stimulated distinct biphasic changes in global PTM profiles (Figure
112 1D). Phase I (0 hr-45 min) was rapid and marked by a trending upregulation of H3K4me2/3,
113 PTMs known to mark transcriptionally active promoters. Phase II (90 min-24 hrs) was

114 characterized by global decreases in di- and tri- histone methylation. Decreased levels of di-
115 and tri-methylated peptides were accompanied by increases in acetylated and unmodified
116 peptide species. Similarly in C57BL/6J mice, histone PTM responses were marked by
117 significant decreases in histone di- and tri-methylation that essentially matched the patterns
118 found in HCT116 cells during the prolonged Phase II response (Figure 1E and Figure S1E-S1J).
119 Decreased higher state (di- and tri-) histone methylation both *in vitro* and *in vivo* highlights a
120 decreased methylation capacity resulting from prolonged Met and/or SAM depletion. Together,
121 these observations suggest perturbed methyl-donor metabolism is capable of stimulating
122 significant changes in histone, but not global 5mC, methylation abundance. Furthermore,
123 similarities between the metabolic and epigenetic responses to Met-restriction across both
124 systems support the use of *in vitro* Met-restriction as a model for mechanistic follow-up studies.
125
126 Decreased SAM Availability Drives Robust Histone Methylation Response
127
128 Dramatic reduction of intracellular Met and SAM correlated with onset of the *in vitro*
129 Phase I and II histone PTM changes, respectively (Figure 1D and Figure S1A-S1B). This
130 implies depletion of individual methyl-metabolites may be capable of stimulating distinct histone
131 modifying pathways. To determine if the global losses in di- and tri- histone methylation *in vitro*
132 are driven specifically by SAM depletion, two alternative approaches were employed to deplete
133 cellular SAM independent of Met (Figure 2A). The first approach utilized RNAi knockdown of the
134 mammalian SAM synthetase MAT2A (methionine adenosyltransferase II alpha). Knockdown via
135 MAT2A-RNAi treatment decreased MAT2A transcript abundance by greater than 97%, resulting
136 in a near complete deprivation of SAM availability with no effect on Met levels (Figure 2B-2D).
137 Histone proteomics analysis of MAT2A-RNAi treated cells identified site-specific histone PTM
138 changes that mirrored those identified in HCT116 cells under Phase II Met-restriction conditions
139 ($r=0.778$, $p=8.59e_{-10}$) (Figure 2E). Using a complementary approach, SAM levels were depleted
140 by overexpression of a major SAM consumer, PEMT (phosphatidylethanolamine N-
141 methyltransferase). Ye et al. 2017 have previously shown PEMT overexpression significantly
142 reduces SAM availability in HEK293T human embryonic kidney cells. Histone proteomics
143 analysis of PEMT overexpressing HEK293T cells identified site-specific PTM changes that
144 paralleled those of Met-restricted controls ($r=0.803$, $p=3.30e_{-8}$) (Figure 2F). Together, two
145 separate means of reducing SAM levels demonstrate SAM reduction alone is sufficient to inhibit
146 the methylation capacity of a cell, inducing dynamic changes in histone PTM abundance.

147 Furthermore, these findings support the use of prolonged Met-restriction as a model of SAM
148 depletion.
149 The similar changes in global histone PTM abundance across four SAM depletion
150 systems were analyzed for the presence of methyl PTMs whose abundances either increased
151 or were unaffected by this metabolic perturbation. Such PTMs would be candidate mediators of
152 an adaptive response to SAM depletion. Unexpectedly, all four SAM depletion systems
153 exhibited identical changes in H3K9 methylation (Figure 2G-2J). SAM depletion stimulated a
154 decrease in H3K9me2/3 with a corresponding increase in H3K9ac/14ac and unmodified
155 peptides while net H3K9me1 abundance was unchanged. Preservation of net H3K9me1 levels
156 in response to SAM depletion was reproducible in Met-restricted MCF7, HEK-293, Panc1, and
157 HepG2 cell lines, as well as in MAT2A-RNAi treated HepA1 cells (Figure S2A-S2F). The robust
158 conservation of H3K9me1 abundance in diverse systems marked by reduced methylation
159 capacity suggest this PTM may be supported by adaptive, active mechanisms.
160
161 H3K9me1 Abundance under SAM Depletion is Driven by *de novo* Methylation
162
163 Global levels of H3K9me1 could be maintained through three distinct mechanisms
164 during SAM depletion: 1.) protection from PTM turnover, 2.) de-methylation of H3K9me2/3,
165 and/or 3.) *de novo* methylation of unmodified H3K9. The decrease in H3K9me2/3 and increase
166 in unmodified H3K9 peptide levels across SAM depletion systems suggest H3K9 can be
167 subjected to facile demethylation while *de novo* methylation appears enzymatically unfavorable.
168 However, *de novo* H3K9 mono-methylation would constitute an active, adaptive response to this
169 metabolic stress that is capable of supporting critical chromatin functions.
170 To investigate the contribution of *de novo* methylation to global H3K9me1 levels, RNAi-
171 mediated repression of five H3K9 HMTs was first performed in Met-replete conditions to
172 determine which enzymes catalyzed a majority of H3K9 mono-methylation reactions in HCT116
173 cells. Repression of HMT expression had significant yet restricted effects, given technical
174 limitations, on H3K9 PTM abundance and suggested Ehmt1/Ehmt2 were the primary H3K9
175 mono-methyltransferases in this system (Figure S3A-S3D). Because repression of HMT
176 expression was intended to be coupled with Met-restriction, RNAi treatment could not be
177 extended to elicit larger changes in PTM abundance as HCT116 cells no longer proliferate
178 beyond 24 hours of Met-restriction (Figure S3E). Therefore, small molecule (UNC0642)
179 inhibition of H3K9 HMTs Ehmt1 and Ehmt2 was used as the best approach to acutely block
180 nuclear H3K9 mono-methylation (Liu F et al., 2013). UNC0642 treatment of Met-replete cells

181 reduced H3K9me1 abundance to a greater extent than RNAi repression of EHMT1/2 (Figure 3A
182 and Figure S3D). Coupling UNC0642 treatment with Met-restriction also stimulated a significant
183 decrease in H3K9me1 levels (Figure 3B and Figure S3F). Comparatively, these data suggest
184 Ehmt1/Ehmt2 retain nearly 60% of their H3K9 mono-methylation activity during severe *in situ*
185 SAM deprivation and that this activity is critical for preserving global H3K9me1 abundance
186 (Figure 3C). Furthermore, H3K9me2 abundance decreased significantly in Met-replete cells
187 upon UNC0642 treatment but was unaffected when UNC0642 was coupled with Met-restriction
188 (Figure 3A-3B). This indicates only the mono-methylation activity of Ehmt1 and Ehmt2 is
189 preferentially supported during SAM depletion.
190 In addition to methylation of H3K9 by nuclear enzymes, mono-methylation is known to
191 be enzymatically catalyzed on cytoplasmic histones prior to nuclear import and deposition onto
192 chromatin (Loyola A et al., 2006; Pinheiro et al., 2012). Subcellular fractionation of Met-
193 restricted HCT116 cells coupled with western blot analyses indicated that cytoplasmic
194 H3K9me1 levels increase 3-fold after 24 hours of Met-restriction, with a similar increase in total
195 H3 protein levels (Figure 3D-3E). To determine the contribution of cytoplasmic H3K9me1 to the
196 chromatin-bound nuclear pool after 24 hours of Met-restriction, a pulse-chase, SILAC
197 experiment was performed (Figure 3F). L-Arg$_{+10}$ isotope incorporation prior to Met-restriction
198 was determined to be nearly complete with average incorporation for H3K9 peptides greater
199 than 98% (Figure S3H). Newly synthesized H3 was calculated to comprise 24% of the
200 chromatin bound histone pool and contributed 18% of the global H3K9me1 signal after 24 hours
201 of Met-restriction (Figure 3G-3H). UNC0642 treatment did not significantly lessen the
202 contribution of cytoplasmic H3K9me1 to the total pool, suggesting cytoplasmic H3K9me1 may
203 be largely protected from enzyme catalyzed turnover once deposited onto chromatin under
204 these conditions (Figure 3H). Modest, insignificant decreases in L-Arg$_{+0}$ H3K9 PTM signal after
205 UNC0642 treatment can be attributed to reduced incorporation of newly synthesized H3 onto
206 chromatin. (Figure 3G) Reduced H3 incorporation in UNC0642-treated cells is likely the
207 consequence of a slower growth rate under these conditions (Figure S3E). Together, these
208 results suggest ~40% of global H3K9me1 abundance is driven by *de novo* methylation during
209 Met-restriction with nearly equal contributions from both the cytoplasm and nucleus. The
210 remaining ~60% of H3K9me1 levels are likely protected from turnover and/or are generated via
211 H3K9me2/3 de-methylation during SAM depletion (Figure 3I).
212 The significant upregulation of cytoplasmic H3K9me1 and total H3, coupled with their
213 incorporation onto chromatin during SAM depletion, were unexpected. These findings suggest
214 cells utilize scarcely available Met and SAM to support the protein abundance and methylation

215 of histone H3 under these conditions. Shotgun proteomics was performed on cytoplasmic
216 protein fractions of the previously described SILAC experiment to determine if histone protein
217 abundance is uniquely responsive to SAM depletion. Of the more than 2,400 identified proteins,
218 only 8 possessed significant incorporation of the light L-Arg$_{+0}$ isotope and also increased in
219 absolute abundance by a $\log_2$ fold-change value greater than 2.0 (Figure 3J). Frequency of Met
220 residues in the primary amino acid sequence did not affect L-Arg$_{+0}$ isotope incorporation (Figure
221 S3I). Remarkably, all four core histone subunits, Mat2A, and the methionine importer SLC3A2
222 (Bröer et al., 2001) were among the 8 proteins (Figure 3J). These results suggest proteins
223 critical for chromatin stability and methyl-donor metabolism are preferentially generated during
224 metabolically-induced SAM depletion. To our knowledge, this is also the first example of a
225 metabolic stress stimulating increased histone protein abundance.
226
227 H3K9me1 is Redistributed Over Repetitive and Transposable Elements During SAM Depletion
228
229 Multiple, non-redundant mechanisms for H3K9me1 maintenance suggest strong
230 biological pressure exists to retain this PTM under SAM depleted conditions. One critical
231 function for H3K9me1 is to serve as a primer for H3K9me2/3 methylation as methyltransferases
232 that yield these higher methylation states require a mono-methyl substrate (Peters et al., 2001;
233 Loyola et al., 2006; Loyola et al., 2009). Accordingly, installment of H3K9me2/3 for constitutive
234 heterochromatin-mediated repression of telomeric, pericentromeric, and centromeric
235 repetitive/transposable elements requires readily available H3K9me1 (Rea et al., 2000;
236 Bannister et al., 2001; Lachner et al., 2000).
237 To determine if H3K9me1 is being maintained globally or redistributed to regions of
238 susceptible heterochromatin during SAM depletion, ChIP-sequencing was performed. Met-
239 restriction stimulated a 35% loss in total H3K9me3 peak abundance (Figure 4A). A higher
240 percentage of H3K9me3 peaks were lost at LTR, intergenic, and intron annotated loci relative to
241 the total, while H3K9me3 enrichment at satellite, simple repeat, and SINE annotated loci were
242 slightly less sensitive to SAM depletion (Figure 4A). Interestingly, H3K9me1 enrichment at
243 repetitive and transposable loci were either largely unaffected by SAM depletion or increased
244 (Figure 4B). Only the percent change for intergenic and intron annotated H3K9me1 peaks was
245 lost to a greater extent than the total peak number, suggesting H3K9me1 is more susceptible to
246 de-methylation at these genomic loci.
247 Maintained or increased levels of H3K9me1 at constitutively repressed regions during
248 SAM depletion could result from the replacement of H3K9me1 for lost H3K9me3. To investigate

249 this possibility, H3K9me1 reads were mapped to nearly $16e_4$ regions determined to lose
250 H3K9me3 peak enrichment upon SAM depletion. This analysis determined H3K9me1
251 enrichment increases at 66.4% of these sites (Figure 4C-4D). A higher percentage of these
252 H3K9me1 enriched sites were annotated for LINE, LTR, simple repeat, and satellite elements
253 relative to those experiencing decreased H3K9me1 read enrichment (Figure 4E). Figure 4F
254 provides a representative image of H3K9me3 replacement by H3K9me1 at a pericentric,
255 repetitive loci. Together, these ChIP-sequencing analyses suggest SAM depletion stimulates
256 the redistribution and targeting of H3K9me1 methylation patterns to repetitive and transposable
257 genomic loci which are susceptible to higher state H3K9 demethylation.
258
259 *De novo* H3K9 Mono-methylation Preserves Heterochromatin Stability
260
261 Replacement of H3K9me3 by H3K9me1 may function to preserve heterochromatin
262 stability and pericentric chromatin repression during SAM depletion by providing the primer for
263 site-specific H3K9me2/3 methylation and/or by preventing H3K9 acetylation. An MNase
264 accessibility assay was used to evaluate global heterochromatin stability under SAM depleted
265 conditions as MNase can more readily digest euchromatic DNA compared to heterochromatic
266 DNA. Coupling Met-restriction with UNC0642 treatment resulted in a significantly greater loss
267 and accumulation of di- and mono-nucleosome species, respectively, compared to Met-
268 restriction alone (Figure 5A-5B). This indicates inhibition of *de novo* H3K9 mono-methylation
269 during SAM depletion has a more detrimental effect on global heterochromatin stability than
270 SAM depletion in isolation. To determine if global decreases in heterochromatin stability
271 resulted in de-repression of transposable DNA elements, RT-qPCR was employed. Transcript
272 abundance of *LINE 1*, *HERV-K*, and *HERV-R* were all significantly elevated after SAM
273 depletion. Coupling SAM depletion with UNC0642 treatment resulted in the further elevation of
274 *LINE1* and *HERV-K* transcript abundance while *HERV-R* expression was unaffected (Figure 5C-
275 5E). Because SAM depletion-induced losses in heterochromatin stability and retrotransposon
276 repression are exacerbated with inhibition of nuclear Ehmt1/Ehmt2 activity, these data suggest
277 stimulation of *de novo* H3K9 mono-methylation functions, in part, to preserve heterochromatin
278 stability.
279
280 Adaptive H3K9 Mechanisms Support Epigenetic Persistence Upon Metabolic Recovery
281

282 Dysregulation of adaptive epigenetic mechanisms during SAM depletion may produce
283 aberrant changes in histone PTMs that compromise long-term epigenetic persistence upon
284 metabolic recovery. To determine if *de novo* H3K9me1 is required for epigenetic persistence to
285 SAM depletion, HCT116 cells were allowed to recover in Met-replete media after being
286 subjected to Met-restriction coupled with acute DMSO or UNC0642 treatment (Figure 6A).
287 Histone proteomics analysis confirmed that inhibition of Ehmt1/Ehmt2 activity during SAM
288 depletion results in a significant loss of H3K9me1 abundance (Figure 6B-6C). Upon 5 and 24
289 hours of Met-repletion, DMSO control cells largely regained their original histone PTM state
290 (Figure 6B). However, histone PTM states of cells acutely treated with UNC0642 only during
291 Met-restriction remained dysregulated after both 5 and 24 hours of Met-repletion (Figure 6B).
292 Although significant global dysregulation was apparent, the H3K9 peptide proteoforms displayed
293 the most dynamic differences (Figure 6D-6E). Interestingly, the signature H3K9 PTM response
294 to SAM depletion described in Figure 2 was largely retained upon Met-repletion in cells acutely
295 treated with UNC0642 (Figure 6D-6E). H3K9me3 abundance was an exception, recovering to
296 levels consistent with regained *LINE 1* and *HERV-K/R* repression (Figure 5C-5E).
297 Met-replete cells allowed to recover from acute UNC0642 treatment also experienced
298 prolonged changes in H3K9 PTM abundance after inhibitor removal (Figure S4A). As Ehmt1/2
299 inhibition by UNC0642 was determined to be reversible (Figure SB-S4C), these results suggest
300 disrupted persistence to small molecule treatment – in either isolation from or conjunction with
301 SAM depletion – is a direct consequence of acute losses in Ehmt1/Ehmt2 activity.
302 To assess the transcriptional consequences of lost epigenetic persistence, RNA-
303 sequencing was performed on cells which recovered in Met-replete media after Met-restriction
304 coupled with acute DMSO or UNC0642 treatment. Principle Component Analysis (PCA) of
305 normalized Transcripts Per Million (TPM) values produced 3 distinct clusters, suggesting altered
306 epigenomes correlate with altered transcript profiles in these cells (Figure 6F). A multiple
307 condition comparison analysis was used to determine which transcripts distinguished the
308 clusters from one another (Figure 6G). While 68.4% of identified genes were ubiquitously
309 expressed across samples (Pattern 1), 27.7% were uniquely expressed in control cells relative
310 to both recovery groups (Pattern 4) (Figure 6H). This result supports the PCA findings as the
311 pre-restriction control group is most distinct from both recovery groups. Unique gene expression
312 profiles for UNC0642 (Pattern 2) and DMSO (Pattern 3) recovery cells contained 1.9% and
313 0.7%, respectively, of all identified genes. Therefore, these subsets of genes are responsible for
314 the unique clustering of both Met-restriction recovery groups (Figure 6H). Gene Set Enrichment
315 Analysis (GSEA) was performed on both Pattern 2 and 3 gene lists to determine functional

316 differences between each gene set. GSEA of Pattern 2 genes identified 71 significantly enriched
317 gene ontology (GO) terms possessing an FDR q-value less than 0.25, while an identical
318 analysis of Pattern 3 genes did not identify any significantly enriched GO terms (Figure 6I-6J).
319 Of the significantly enriched GO terms in Pattern 2, 66 possessed a positive Normalized
320 Enrichment Score (NES) when comparing UNC0642 to DMSO control recovery cells (Figure
321 S5A-S5B). Figure 6K is a representative GSEA running enrichment score figure of a GO term
322 possessing a positive NES. Only 5 of the significantly enriched GO terms in Pattern 2
323 possessed a negative NES when comparing UNC0642 to DMSO control recovery cells.
324 Notably, a majority of the genes assigned to these GO terms were zinc finger binding proteins
325 (Figure S5C-S5D). Figure 6L is a representative GSEA running enrichment score figure of a GO
326 term possessing a negative NES.
327 These data suggest adaptive regulation of H3K9 PTMs in response to SAM depletion is
328 required for long-term epigenetic persistence upon metabolic recovery. Furthermore, inhibited
329 epigenetic persistence results in significant transcriptional consequences that impact a diverse
330 set of cellular functions.
331
332 Adaptive and Persistent Epigenetic Responses to SAM Depletion are Robust *in vivo*,
333 Independent of Age
334
335 To determine if adaptive and persistent responses to SAM depletion exist *in vivo* and are
336 age-independent, 6- and 22-month C57BL/6J mice were subjected to 3 weeks of Met-restriction
337 followed by 5 weeks of Met-repletion (Figure 7A). Several previous reports have associated
338 decreased H3K9me2/3 abundance with aging in numerous organisms (Wood et al., 2010;
339 Larson et al., 2012; Ni et al., 2012; Tvardovskey et al., 2017; Scaffidi and Misteli, 2006). Age-
340 dependent dysregulation of heterochromatin has been associated with de-repression of
341 repetitive DNA and transposable elements, as well as DNA damage, factors which may
342 contribute to disease progression (Wood et al., 2016; De Cecco et al., 2013; De Cecco et al.,
343 2019; Oberdoerffer and Sinclair, 2007; Booth and Brunet, 2016). Therefore, conservation of
344 both adaptive and persistent responses to SAM depletion across the lifespan would further
345 support the functional importance of both mechanisms as an “older” chromatin environment is
346 thought to be inherently dysregulated.
347 Remarkably, histone proteomics analysis of liver tissue revealed H3K9 was the only
348 residue on which PTMs responded similarly to SAM depletion in both 6- and 22-month mice
349 relative to age-matched controls (Figure 7B). This PTM response at H3K9 phenocopied those

350 identified in the previously described *in vitro* and whole-organism SAM depletion studies, further
351 highlighting the robust regulation of this residue (Figure 7C). Significant age-dependent
352 responses to SAM depletion were identified on all remaining histone residues (Figure 7B and
353 S6A-S6E). Furthermore, significantly elevated *LINE 1*, *SINE B1*, and *SINE B2* transcript
354 abundance in both 6- and 22-month mice suggest the chromatin instability phenotype
355 characterized in Figure 5 also occurs during metabolic depletion of SAM *in vivo* (Figure 7D-7E).
356 After 5 weeks of dietary Met-reintroduction, both young and old mice displayed the ability to re-
357 establish an epigenome similar to that possessed by age-matched controls (Figure 7B).
358 Interestingly, 22-month mice appeared to more rapidly adopt the control histone PTM state,
359 while the 6-month mice still exhibited residual losses in H3K9me3 and increases in H3K9me1
360 after 5 weeks of recovery (Figure 7F). Consistent with the general recovery of chromatin states,
361 both age groups largely reestablished repression of *LINE 1*, *SINE B1*, and *SINE B2* expression
362 (Figure 7G-7H).
363 Metabolic changes in young and old mice tracked with H3K9 PTMs. Both 6- and 22-
364 month mice in the Met-restriction group experienced significant losses in total body weight
365 relative to age matched controls (Figure S6F). Decreases in overall body weight were
366 comprised of significant losses in both lean and fat mass (Figure S6F). Altered body-weight and
367 compositions were accompanied by significantly improved glucose tolerance in both young and
368 old mice (Figure S6G). Upon Met-repletion, mice reacquired their initial metabolic state in an
369 age-independent manner. All animals experienced significant increases in total body weight,
370 comprised of elevated lean and fat mass, as well normalized glucose tolerance relative to age-
371 matched controls (Figure S6H-S6I).
372 Together, strong association of the H3K9 chromatin response to SAM depletion with
373 metabolic reprogramming in young and old mice suggest H3K9 regulatory mechanisms are not
374 only robust across lifespan but may be required to support these metabolic phenotypes.
375 Furthermore, these data show the ability of epigenetic states to persist upon recovery from a
376 metabolic challenge is an inherent property of both isolated cells and complex mammals.
377
378 **Discussion**
379
380 Here, we provide a comprehensive investigation into the adaptive regulation of
381 chromatin during a metabolic stress. A highly conserved, robust histone methylation response to
382 SAM depletion was discovered, characterized by global losses in histone H3 di- and tri-
383 methylation while H3K9me1 is actively maintained to safeguard against exacerbated

384 heterochromatin instability and support epigenetic persistence upon metabolic recovery. These
385 mechanisms involve the enrichment of H3K9me1 in susceptible regions of heterochromatin
386 through *de novo* methylation of both chromatin-bound and cytoplasmic H3. To our knowledge,
387 this is the first identified mechanism in which scarce, diet-derived nutrients are funneled toward
388 the preservation of specific chromatin PTM states.

389 Zee et al., 2010 have previously determined H3K9me1 has the shortest half-life of 17
390 measured PTMs, highlighting the importance of *de novo* methylation for supporting global
391 H3K9me1 abundance in a SAM depleted environment. Here, *de novo* methylation was found to
392 be critical for more than simply sustaining global H3K9me1 levels under these conditions. ChIP-
393 sequencing analyses determined H3K9me1 patterns experience a significant redistribution
394 across heterochromatin that results in H3K9me1 enrichment at repetitive and transposable DNA
395 elements, particularly in regions where H3K9me3 is lost. Targeting of H3K9me1 to these
396 regions is likely critical for preserving heterochromatin as prevention of *de novo* H3K9 mono-
397 methylation resulted in global losses in heterochromatin stability and site-specific
398 retrotransposon derepression. We hypothesize H3K9me1 facilitates repression of
399 retrotransposons during SAM depletion through two simultaneous mechanisms: 1.) acting as
400 the primed substrate for HMTs which deposit di- and tri-methyl PTMs onto H3K9 (Peters et al.,
401 2001; Loyola et al., 2006; Loyola et al., 2009; Rea et al., 2000; Bannister et al., 2001; Lachner
402 et al., 2000) and 2.) preventing the acetylation of newly demethylated H3K9 residues. Increased
403 H3K9 acetylation through impaired H3K9 deacetylation pathways is associated with global
404 genomic instability as well as derepression of LINE1, providing support for the second
405 mechanism (Mostoslavsky et al., 2006; Van Meter et al., 2014; Simon et al., 2019). Ensuring
406 sufficient amounts of H3K9me1 are available to facilitate heterochromatin stability is not limited
407 to nuclear derived H3K9me1. Pinheiro et al., 2012 have previously shown inhibition of
408 cytoplasmic H3K9 mono-methylation through shRNA knockdown of *PRDM3* and *PRDM16*
409 stimulates pericentric heterochromatin loss and disruption of the nuclear lamina. Our study
410 demonstrates cytoplasmic derived H3K9me1 comprises a significant portion (18%) of the total
411 chromatin bound pool after 24 hours of Met-restriction *in vitro*. Adaptation of H3K9 mono-
412 methylation to SAM depletion is also critical for long-term epigenetic persistence to this
413 metabolic stress. Prevention of *de novo* H3K9 mono-methylation during SAM depletion resulted
414 in sustained dysregulation of global histone PTMs upon metabolic recovery, significantly
415 influencing gene expression patterns. This requirement for an active, adaptive histone PTM
416 response to support epigenetic persistence upon metabolic recovery is the first identified
417 mechanism of its kind.

418 Replication of *in vitro* results *in vivo*, independent of age, strongly supports the discovery
419 of a universal adaptive and persistent response to SAM depletion. Here, we demonstrate that
420 the adaptive mechanisms required to support H3K9me1-mediated heterochromatin stability are
421 inducible in both 6- and 22-month mice after dietary Met-restriction. Furthermore, H3K9me1
422 maintenance under SAM depleted conditions uniquely correlated with beneficial metabolic
423 reprogramming (i.e. reduced fat mass and improved glucose tolerance) in both young and old
424 mice. This suggests the robust regulation of H3K9 PTMs in response to SAM depletion may be
425 required to support the metabolic reprogramming stimulated by dietary Met-restriction. Global
426 epigenetic persistence to metabolic SAM depletion was observed in both 6- and 22-month mice.
427 Validation of this phenomenon *in vivo*, independent of age, suggests similar mechanisms critical
428 for maintaining proper regulation of the epigenome during life-experienced fluctuations in the
429 availability of other metabolic cofactors may exist as well. Such fluctuations could be stimulated
430 by periods of prolonged fasts, chronic intake of foods lacking essential cofactors (i.e. vegan and
431 vegetarian dietary patterns), and circadian regulated changes in metabolite availability (Farmer,
432 2014; Schmidt et al., 2016; Krishnaiah et al., 2017).
433 Notably, we did not observe an age-associated decrease in H3K9 methylation between
434 6- and 22-month control diet mice (Table S1). Similar regulation of H3K9 PTMs and mirrored
435 metabolic responses to SAM depletion across age groups suggest our 22-month mice, the
436 equivalent to a 60-70 year old human, have not yet experienced a decline in health-span
437 (Flurkey et al., 2007). It will be interesting to determine if the adaptive and persistent epigenetic
438 mechanisms revealed here are functional in very old animals (i.e. >30 months) where H3K9
439 methylation is thought to be inherently dysregulated. Disruption of these mechanisms later in an
440 organism's lifespan could support age-associated derepression of transposable elements
441 (Wood et al., 2016; De Cecco et al., 2013; Oberdoerffer and Sinclair, 2007; Booth and Brunet,
442 2016), contributing to negative phenotypes that accelerate the aging process such as
443 inflammation (De Cecco et al., 2019; Simon et al., 2019).
444 Future studies will be needed to determine how H3K9 mono-methyltransferases are able
445 to maintain their catalytic activity in SAM depleted environments. Favorable steady-state kinetic
446 constants for H3K9me1 relative to H3K9me2/3 HMTs is one possibility. However, it is difficult to
447 address this hypothesis by comparing existing literature on H3K9 HMT enzymology, due to
448 disparate substrates and assays. Direct shuttling of SAM to H3K9me1 HMTs by Mat2A could
449 also support H3K9me1 HMT catalytic activity. As SAM is energetically expensive to produce,
450 due to the 1:1 requirement of Met and ATP molecules for its synthesis, in addition to being
451 highly unstable (Wu et al., 1983), it would be advantageous for the cell to possess mechanisms

452 which permit preferential shuttling of SAM during methyl-metabolite depletion. Directed SAM
453 production and utilization have been proposed in other metabolic contexts (Katoh et al., 2011;
454 Kera et al., 2013; Li et al., 2015).
455
456 **Acknowledgements**
457
458 This research was supported in part by grants from the NIH (S.A.H. –T32 DK007665; K.A.K.
459 T32 DK007665; W.H.L. T32 DK007665; J.M.D. – R37 GM059785; D.W.L. – AG041765,
460 AG050135, AG051974, AG056771, AG062328, a New Investigator Program Award (D.W.L.)
461 and a Collaborative Health Sciences Program Award (V.L.C.) from the Wisconsin Partnership
462 Program, the V. Foundation for Cancer Research (V.L.C.), and a Glenn Foundation Award for
463 Research in the Biological Mechanisms of Aging (D.W.L.), as well as startup funds from the
464 UW-Madison School of Medicine and Public Health and the UW-Madison Department of
465 Medicine (V.L.C. and D.W.L.). This research was conducted while D.W.L. was an AFAR
466 Research Grant recipient from the American Federation for Aging Research. D.Y. is supported
467 in part by a fellowship from the American Heart Association (17PRE33410983). The Lamming
468 laboratory is supported in part by the U.S. Department of Veterans Affairs (I01-BX004031), and
469 this work was supported using facilities and resources from the William S. Middleton Memorial
470 Veterans Hospital. This work does not represent the views of the Department of Veterans
471 Affairs or the United States Government. We would like to thank Alexis J. Lawton for the
472 bioinformatics analysis presented in Figure S3I. We would also like to thank the University of
473 Wisconsin-Madison Biotechnology Center and the University of Wisconsin-Madison Center for
474 High Throughput Computing for their help in generating and analyzing the ChIP-sequencing
475 data presented in Figure 5, respectively.
476
477 **Author Contributions**
478
479 Conceptualization, S.A.H., D.W.L, V.L.C., and J.M.D.; Methodology, S.A.H., C.Y., C.K.W.,
480 L.N.C., W.H.L., K.I., B.P.T., D.W.L., and J.M.D.; Validation, S.A.H., D.Y., C.Y., L.N.C., K.A.K.,
481 K.I., B.P.T., D.W.L., and J.M.D.; Formal Analysis, S.A.H., D.Y., C.K.W., K.A.K., D.W.L., and
482 J.M.D; Investigation, S.A.H., D.Y., C.Y., L.N.C., K.A.K., J.L.T., S.E.Y., and B.R.M.; Resources,
483 K.I., B.P.T., V.L.C., D.W.L., and J.M.D.; Writing – Original Draft, S.A.H. and J.M.D.; Writing –
484 Review & Editing, S.A.H., D.Y., C.Y., C.K.W., W.H.L., K.I., R.S., B.P.T., V.L.C., D.W.L., and
485 J.M.D.; Visualization, S.A.H., D.Y., and D.W.L.; Supervision and Project Administration, K.I.,

R.S., B.P.T., D.W.L., and J.M.D.; Funding Acquisition, S.A.H., K.I., R.S., B.P.T., V.L.C., D.W.L., and J.M.D.

Declaration of Interests

J.M.D. is a consultant for FORGE Life Sciences and co-founder of Galilei BioSciences. D.W.L has received funding from, and is a scientific advisory board member of, Aeonian Pharmaceuticals, which seeks to develop novel, selective mTOR inhibitors for the treatment of various diseases. Remaining authors declare no competing interest.

496 **References**

497

498 1. Arriola Apelo, S.I., Neuman, J.C., Baar, E.L., Syed, F.A., Cummings, N.E., Brar, H.K.,
499 Pumper, C.P., Kimple, M.E., and Lamming, D.W. (2016) Alternative rapamycin treatment
500 regimens mitigate the impact of rapamycin on glucose homeostasis and the immune
501 system. Aging Cell. 15, 28-38.
502 2. Bannister, A.J., Zegerman, P., Pardridge, J.F., Miska, E.A., Thomas, J.O., Allshire, R.C.,
503 and Kouzarides, T. (2001) Selective recognition of methylated lysine 9 on histone H3 by
504 the HP1 chromo domain. Nature. 410, 120-124.
505 3. Bolger, A.M., Lohse, M., and Usadel, B. (2014) Trimmomatic: a flexible trimmer for
506 Illumina sequence data. Bioinformatics. 30, 2114-2120.
507 4. Booth, L.N. and Brunet, A. (2016) The aging epigenome. Mol. Cell. 62, 728-744.
508 5. Bröer, A., Friedrich, B., Wagner, C.A., Fillon, S., Ganapathy, V., Lang, F., and Bröer, S.
509 (2001) Association of 4F2hc with light chains LAT1, LAT2 or y+LAT2 requires different
510 domains. Biochem J. 355, 735-731.
511 6. Brown-Borg, H.M., Rakoczy, S., Wonderlich, J.A., Borg, K.E., and Rojanathammanee, L.
512 (2018) Metabolic adaptation of short-living growth hormone transgenic mice to
513 methionine restriction and supplementation. Ann. N.Y. Acad. Sci. 1418, 118-136.
514 7. Clasquin, M.F., Melamud, E., and Rabinowitz, J.D. (2012) LC-MS processing with
515 MAVEN: a metabolomic analysis and visualization engine. Curr. Protoc. Bioinformatics.
516 Chapter 14, Unit 14.11. doi:10.1002/0471250953.bi1411s37.
517 8. Cox, J., Hein, M.Y., Luber, C.A., Paron, I., Nagaraj, N., and Mann, M. (2014) Accurate
518 proteome-wide label-free quantification by delayed normalization and maximal peptide
519 ratio extraction, termed MaxLFQ. Mol. Cell Proteomics. 13, 2513-2526.
520 9. De Cecco, M., Criscione, S.W., Peckham, E.J., Hillenmeyer, S., Hamm, E.A.,
521 Manivannan, J., Peterson, A.L., Kreiling, J.A., Neretti, N., and Sedivy, J.M. (2013)
522 Genomes of replicatively senescent cells undergo global epigenetic changes leading to
523 gene silencing and activation of transposable elements. Aging Cell. 12, 247-256.
524 10. De Cecco, M., Ito, T., Petrashen, A.P., Elias, A.E., Skivr, N.J., Criscione, S.W.,
525 Caligiana, A., Brocculi, G., Adney, E.M., Boeke, J.D., Le, O., Beauséjour, C., Ambati, J.,
526 Ambati, K., Simon, M., Seluanov, A., Gorbunova, V., Slagboom, P.E., Helfand, S.L.,
527 Neretti, N., and Sedivy, J.M. (2019) L1 drives IFN senescent cells and promotes age-
528 associated inflammation. Nature. 566, 73-78.

529 11. Ding, W., Smulan, L.J., Hou, N.S., Taubert, S., Watts, J.L., and Walker, A.K. (2015) S-
530 adenosylmethionine levels govern innate immunity through distinct methylation-
531 dependent pathways. Cell Metab. 22, 633-645.
532 12. Ducker, G.S. and Rabinowitz, J.D. (2017) One-carbon metabolism in health and
533 disease. Cell Metab. 25, 27-42.
534 13. Fan, J., Krautkramer, K.A., Feldman, J.L., and Denu, J.M. (2015) Metabolic regulation of
535 histone post-translational modifications. ACS Chem. Biol. 10, 95-108.
536 14. Farmer, B. (2014) Nutritional adequacy of plant-based diets for weight management:
537 observations from the NHANES. Am. J. Clin. Nutr. 100 Suppl 1, 365S-368S.
538 15. Flurkey, K., Currer, J.M., and Harrison, D.E. (2007) The Mouse in Aging Research. In
539 the Mouse in Biomedical Research 2nd Edition. Fox, J.G., et al., editors. American
540 College Laboratory Animal Medicine (Elsevier), pp. 637-671.
541 16. Green, C.L. and Lamming, D.W. (2018) Regulation of metabolic health by essential
542 dietary amino acids. Mech. Ageing Dev. S0047-6374(18)30079-4. doi:
543 0.1016/j.mad.2018.07.004.
544 17. Greer, E.L. and Shi, Y. (2012) Histone methylation: a dynamic mark in health, disease,
545 and inheritance. Nat. Rev. Genet. 13, 343-357.
546 18. Hardies, S.C., Wang, L., Zhou, L., Zhao, Y., Casavant, N.C., and Huang, S. (200) LINE-
547 1 (L1) lineages in the mouse. Mol. Biol. Evol. 17, 616-628.
548 19. Hayashi, T., Teruya, T., Chaleckis, R., Morigasaki, S., and Yanagida, M. (2018) S-
549 adenosylmethionine synthetase is required for cell growth, maintenance of G0 phase,
550 termination of quiescence in fission yeast. iScience 5, 38-51.
551 20. Heinz, S., Benner, C., Spann, N., Bertolino, E., Lin, Y.C., Laslo, P., Cheng, J.X., Murre,
552 C., Singh, H., and Glass, C.K. (2010) Simple combinations of lineage-determining
553 transcription factors prime cis-regulatory elements required for macrophage and B cell
554 identities. Mol. Cell. 38, 576-589.
555 21. Kang, Y.K., Park, J.S., Lee, C.S., Yeom, Y.I., Chung, A.S., and Lee, K.K. (1999) Efficient
556 integration of short interspersed element-flanked foreign DNA via homologous
557 recombination. J. Biol. Chem. 274, 36585-36591.
558 22. Katoh, Y., Ikura, T., Hoshikawa, Y., Tashiro, S., Ito, T., Ohta, M., Kera, Y., Noda, T., and
559 Igarashi, K. (2011) Methionine adenosyltransferase II serves as a transcriptional
560 corepressor of Maf oncoprotein. Mol. Cell. 41, 554-566.

561 23. Kera, Y., Katoh, Y., Ohta, M., Matsumoto, M., Takano-Yamamoto, T., and Igarashi, K.
562 (2013) Methionine adenosyltransferase II-dependent histone H3K9 methylation at the
563 COX-2 gene locus. J. Biol. Chem. 288, 13592-13601.
564 24. Klawitter, S., Fuchs, N.V., Upton, K.R., Upton, K.R., Muñoz-Lopez, M., Shukla, R.,
565 Wang, J., Garcia-Cañadas, M., Lopez-Ruiz, C., Gerhardt, D.J., Sebe, A., Grabundzija, I.,
566 Merkert, S., Gerdes, P., Pulgarin, J.A., Bock, A., Held, U., Witthuhn, A., Haase, A.,
567 Sarkadi, B., Löwer, J., Wolvetang, E.J., Martin, U., Ivics, Z., Izsvák, Z., Garcia-Perez,
568 J.L., Faulkner, G.J., and Schumann, G.G. (2016) Reprogramming triggers endogenous
569 L1 and Alu retrotransposition in human induced pluripotent stem cells. Nat. Commun.
570 7:10286. doi: 10.1038/ncomms10286.
571 25. Konze, K.D., Ma, A., Li, F., Barsyte-Lovejoy, D., Parton, T., Macnevin, C.J., Liu, F., Gao,
572 C., Huang, X.P., Kuznetsova, E., Rougie, M., Jiang, A., Pattenden, S.G., Norris, J.L.,
573 James, L.I., Roth, B.L., Brown, P.J., Frye, S.V., Arrowsmith, C.H., Hahn, K.M., Wang,
574 G.G., Vedadi, M., and Jin, J. (2013) An orally bioavailable chemical probe of lysine
575 methyltransferases EZH2 and EZH1. ACS Chem. Biol. 8, 1324-1334.
576 26. Krishnaiah, S.Y., Wu, G., Altman, B.J., Growe, J., Rhoades, S.D., Coldren, F.,
577 Venkataraman, A., Olarerin-George, A.O., Francey, L.J., Mukherjee, S., Girish, S.,
578 Selby, C.P., Cal, S., Er, U., Sianati, B., Sengupta, A., Anafi, R.C., Kavakli, I.H., Sancar,
579 A., Baur, J.A., Dang, C.V., Hogenesch, J.B., and Weljie, A.M. (2017) Clock regulation of
580 metabolites reveals coupling between transcription and metabolism. Cell Metab. 35,
581 961-974.
582 27. Lachner, M., O'Carroll, D., Rea, S., Mechtler, K., and Jenuwein, T. (2001) Methylation of
583 histone H3 lysine 9 creates a binding site for HP1 proteins. Nature. 410, 116-120.
584 28. Larson, K., Yan, S.J., Tsurumi, A., Liu, J., Zhou, J., Gaur, K., Guo, D., Eickbush, T.H.,
585 and Li, W.X. (2012) Heterochromatin formation promotes longevity and represses
586 ribosomal RNA synthesis. PLoS Genet. 8, e1002473. doi:
587 10.1371/journal.pgen.1002473.
588 29. Lees, E.K., Król, E., Grant, L., Shearer, K., Wyse, C., Moncur, E., Bykowska, A.S.,
589 Mody, N., Gettys, T.W., and Delibegovic, M. (2014) Methionine restriction restores a
590 younger metabolic phenotype in adult mice with alterations in fibroblast growth factor 21.
591 Aging Cell. 13, 817-827.
592 30. Leng, N., Dawson, J.A., Thomson, J.A., Ruotti, V., Rissman, A.I., Smits, B.M., Haag,
593 J.D., Gould, M.N., Stewart, R.M., and Kendziorski, C. (2013) EBSeq: an empirical Bayes
594 hierarchical model for inference in RNA-seq experiments. Bioinformatics. 29, 1035-1043.

595 31. Li, H., Handsaker, B., Wysoker, A., Fennell, T., Ruan, J., Homer, N., Marth, G.,
596 Abecasis, G., Durbin, R., and 1000 Genome Project Data Processing Subgroup. (2009)
597 The sequence alignment/map format and SAMtools. Bioinformatics. 25, 2078-2079.
598 32. Li, B. and Dewey, C.N. (2011) RSEM: accurate transcript quantification from RNA-Seq
599 data with or without a reference genome. BMC Bioinform. doi: 10.1186/1471-2105-12-
600 323.
601 33. Li, S., Swanson, S.K., Gogol, M., Florens, L., Washburn, M.P., Workman, J.L, and
602 Suganuma, T. (2015) Serine and SAM responsive complex SESAME regulates histone
603 modification crosstalk by sensing cellular metabolism. Mol. Cell. 60, 408-421.
604 34. Li, X., Egervari, G., Wang, Y., Berger, S.L., and Lu, Z. (2018) Regulation of chromatin
605 and gene expression by metabolic enzymes and metabolites. Nat. Rev. Mol. Cell Biol.
606 19, 563-578.
607 35. Liu, F., Barsyte-Lovejoy, D., Li, F., Xiong, Y., Korboukh, V., Huang, X.P., Allali-Hassani,
608 A., Janzen, W.P., Roth, B.L., Frye, S.V., Arrowsmith, C.H., Brown, P.J., Vedadi, M., and
609 Jin, J. (2013) Discovery of an in vivo chemical probe of the lysine methyltransferases
610 G9a and GLP. J. Med. Chem. 56, 8931-8942.
611 36. Loyola, A., Bonaldi, T., Roche, D., Imhof, A., and Almouzni, G. (2006) PTMs on H3
612 variants before chromatin assembly potentiate their final epigenetic state. Mol. Cell. 24,
613 309-316.
614 37. Loyola, A., Tagami, H., Bonaldi, T., Roche, D., Quivy, J.P., Imhof, A., Nakatani, Y., Dent,
615 S.Y. and Almouzni, G. (2009) The HP1α-CAF1-SETDB1-containing complex provides
616 H3K9me1 for Suv39-mediated K9me3 in pericentric heterochromatin. Embo Rep. 10,
617 769-775.
618 38. MacLean, B., Tomazela, D.M., Shulman, N., Chamber, M., Finney, G.L., Frewen, B.,
619 Kern, R., Tabb, D.L., Liebler, D.C., and MacCoss, M.J. (2010) Skyline: an open source
620 document editor for creating and analyzing targeted proteomics experiments.
621 Bioinformatics. 26, 966-968.
622 39. Mauger, O., Klinck, R., Chabot, B., Muchardt, C., Allemand, E., and Batsché, E. (2015)
623 Alternative splicing regulates the expression of G9A and SUV39H2 methyltransferases,
624 and dramatically changes SUV39H2 functions. Nucleic Acids Res. 43, 1869-1882.
625 40. Melamud, E., Vastag, L, and Rabinowitz, J.D. (2010) Metabolomic analysis and
626 visualization engine for LC-MS data. Anal. Chem. 82, 9818-9826.
627 41. Mentch S.J. and Locasale J.W. (2016) One-carbon metabolism and epigenetics:
628 understanding the specificity. Ann N. Y. Acad. Sci. 1363, 91-98.

629 42. Mentch, S.J., Mehrmohamadi, M., Huang, L., Liu, X., Gupta, D., Mattocks, D., Gómez
630 Padilla, P., Ables, G., Bamman, M.M., Thalacker-Mercer, A.E. Nichenametla, S.N., and
631 Locasale, J.W. (2015) Histone methylation dynamics and gene regulation occur through
632 the sensing of one-carbon metabolism. Cell Metab. 22,861-873.
633 43. Miller, R.A., Buehner, G., Chang, Y., Harper, J.M., Sigler, R., and Smith-Wheelock, M.
634 (2005) Methionine-deficient diet extends mouse lifespan, slows immune and lens aging,
635 alters glucose, T4, IGF-I and insulin levels, increases hepatocyte MIF levels and stress
636 resistance. Aging Cell. 4, 119-125.
637 44. Mootha, V.K., Lindgren, C.M., Eriksson, K.F., Subramanian, A., Sihag, S., Lehar, J.,
638 Puigserver, P., Carlsson, E., Ridderstråle, M., Laurila, E., Houstis, N., Daly, M.J.,
639 Patterson, N., Mesirov, J.P., Golub, T.R., Tamayo, P., Spiegelman, B., Lander, E.S.,
640 Hirschhorn, J.N., Altshuler, D., and Groop, L.C. (2003) PGC-1alpha responsive genes
641 involved in oxidative phosphorylation are coordinately downregulated in human diabetes.
642 Nat. Genet. 34, 267-273.
643 45. Mostoslavsky, R., Chua, K.F., Lombard, D.B., Pang, W.W., Fischer, M.R., Gellon, L.,
644 Liu, P., Mostoslavsky, G., Franco, S., Murphy, M.M., Mills, K., Patel, P., Hsu, J.T., Hong,
645 A.L., Ford, E., Cheng, H.L., Kennedy, C., Nunez, N., Bronson, R., Frendewey, D.,
646 Auerbach, W., Valenzuela, D., Karow, M., Hottiger, M.O., Hursting, S., Barret, J.C.,
647 Guarente, L., Mulligan, R., Demple, B., Yancopoulos, G.D., and Alt, F.W. (2006)
648 Genomic instability and aging-like phenotype in the absence of mammalian SIRT6. Cell.
649 124, 315-329.
650 46. Ni, Z., Ebata, A., Alipanahiramandi E., and Lee, S.S. (2012) Two SET domain containing
651 genes link epigenetic changes and aging in Caenorhabditis elegans. Aging Cell. 11, 315-
652 325.
653 47. Northcott, P.A., Nakahara, Y., Wu, X., Feuk, L., Ellison, D.W., Croul, S., Mack, S.,
654 Kongkham, P.N., Peacock, J., Dubuc, A., Ra, Y.S., Zilberberg, K., Mcleod, J., Scherer,
655 S.W., Rao, J.S., Eberhart, C.G., Grajkowska, W., Gillespie, Y., Lach, B., Grundy, R.,
656 Pollack, I.F., Hamilton, R.L., Van Meter, T., Carlotti, C.G., Boop, F., Bigner, D.,
657 Gilbertson, R.J., Rutka, J.T., and Taylor, M.D. (2009) Multiple recurrent genetic events
658 converge on control of histone lysine methylation in medulloblastoma. Nat. Genet. 41,
659 465-472.
660 48. Oberdoerffer, P. and Sinclair, D.A. (2007) The role of nuclear architecture in genome
661 instability and ageing. Nat. Rev. Mol. Cell Biol. 8, 692-702.

662 49. Orentreich, N., Matias, J.R., DeFelice, A., and Zimmerman, J.A. (1993) Low methionine
663 ingested by rats extends life span. J. Nutr. 123, 269-274.
664 50. Peters, A.H., O'Carroll, D., Scherthan, H., Mechtler, K., Sauer, S., Schöfer, C.,
665 Weipoltshammer, K., Pagani, M., Lachner, M., Kohlmaier, A., Opravil, S., Doyle, M.,
666 Sibilia, M., and Jenuwein, T. (2001) Loss of the Suv39h histone methyltransferase
667 impairs mammalian heterochromatin and genome stability. Cell. 107, 323-327.
668 51. Pinheiro, I., Margueron, R., Shukeir, N., Eisold, M., Fritzsch, C., Richter, F.M., Mittler, G.,
669 Genoud, C., Goyama, S., Kurokawa, M., Son, J., Reinberg, D., Lachner, M., and
670 Jenuwein, T. (2012) Prdm3 and Prdm16 are H3K9me1 methyltransferases required for
671 mammalian heterochromatin integrity. Cell. 150, 948-960.
672 52. Qi, F., Shang, K., Zhang, J., Chuai, S., Kong, D., Zhou, T., Fu, S., Liang, Y., Li, C.,
673 Chen, Z., Zhao, Y., Yu, Z., Huang, Z., Hu, M., Ying, H., Chen, Z., Zhang, Y., Xing, F.,
674 Zhu, J., Xu, H., Zhao, K., Lu, C., Atadja, P., Xia, Z.X., Li, E., and Shou, J. (2015) Histone
675 methyltransferase SETDB1 regulates liver cancer cell growth through methylation of
676 p53. Nat. Commun. 6, 8651.
677 53. Quinlan, A.R. and Hall, I.M. (2010) BEDTools: a flexible suite of utilities for comparing
678 genomic features. Bioinformatics. 26, 841-842.
679 54. Rea S., Eisenhaber, F., O'Carroll, D., Strahl, B.D., Sun, Z.W., Schmid, M., Opravil, S.,
680 Mechtler, K., Pontin, C.P., Allis, C.D., and Jenuwein, T. (2000) Regulation of chromatin
681 structure by site-specific histone H3 methyltransferases. Nature. 406, 593-599.
682 55. Rhyu, D.W., Kang, Y.J., Ock, M.S., Eo, J.W., Choi, Y.H., Kim, W.J., Leem, S.H., Yi, J.M.,
683 Kim, H.S., and Cha, H.J. (2014) Expression of human endogenous retrovirus env genes
684 in the blood of breast cancer patients. Int. J. Mol. Sci. 15, 9173-9183.
685 56. Scaffidi, P. and Misteli, T. (2006) Lamin A-dependent nuclear defects in human aging.
686 Science. 312, 1059-1063.
687 57. Schmidt, J.A., Rinaldi, S., Scalber, A., Ferrari, P., Achaintre, D., Gunter, M.J., Appleby,
688 P.N., Key, T.J., and Travis, R.C. (2016) Plasma concentrations and intakes of amino
689 acids in male meat-eaters, fish-eaters, vegetarians and vegans: a cross-sectional
690 analysis in EPIC-Oxford cohort. Eur. J. Clin. Nutr. 70, 306-312.
691 58. Shiraki, N., Shiraki, Y., Tsuyama, T., Obata, F., Miura, M., Nagae, G., Aburatani, H.,
692 Kume, K., Endo, F., and Kume, S. (2014) Methionine metabolism regulates maintenance
693 and differentiation of human pluripotent stem cells. Cell Metab. 19, 780-794.
694 59. Shyh-Chang, N., Locasale, J.W., Lyssiotis, C.A., Zheng, Y., Teo, R.Y.,
695 Ratanasirintrawoot, S., Zhang, J., Onder, T., Unternaehrer, J.J., Zhu, H., Asara, J.M.,

696 Daley, G.Q., and Cantley, L.C. (2013) Influence of threonine metabolism on S-
697 adonsylmethionine and histone methylation. Science. 339, 222-226.
698 60. Simon, M., Van Meter, M., Ablaeva, J., Ke, Z., Gonzalez, R.S., Taguchi, T., De Cecco,
699 M., Leonova, K.I., Kogan, V., Helfand, S.L., Neretti, N., Roichman, A., Cohen, H.Y.,
700 Meer, M.V., Gladyshev, V.N., Antoch, M.P., Gudkov, A.V., Sedivy, J.M., Seluanov, A.,
701 and Gorbunova, V. (2019) LINE1 derepression in aged wild-type and SIRT6-deficient
702 mice drives inflammation. Cell Metab. 29, 871-885.
703 61. Strekalova, E., Malin, D., Weisenhorn, E.M.M., Russell, J.D., Hoelper, D., Jain, A., Coon,
704 J.J., Lewis, P.W., and Cryns, V.L. (2019) S-adenosylmethionine biosynthesis is a
705 targetable metabolic vulnerability of cancer stem cells. Breast Cancer Res. Treat. 175,
706 39-50.
707 62. Subramanian, A., Tamayo, P., Mootha, V.K., Mukherjee, S., Ebert, B.L., Gillette, M.A.,
708 Paulovich, A., Pomeroy, S.L., Golub, T.R., Lander, E.S., and Mesirov, J.P. (2005) Gene
709 set enrichment analysis: a knowledge-based approach for interpreting genome-wide
710 expression profiles. Proc. Natl. Acad. Sci.102, 15545-15550.
711 63. Tang, S., Fang, Y., Huang, G., Xu, X., Padilla-Banks, E., Fan, W., Xu, Q., Sanderson,
712 S.M., Foley, J.F., Dowdy, S., McBurney, M.W., Fargo, D.C., Williams, C.J., Locasale,
713 J.W., Guan, Z., and Li, X. (2017) Methionine metabolism is essential for SIRT1-regulated
714 mouse embryonic stem cell maintenance and embryonic development. EMBO J. 36,
715 3175-3193.
716 64. Tang, X., Keenan, M.M., Wu, J., Lin, C.A., Dubois, L., Thompson, J.W., Freedland, S.J.,
717 Murphy, S.K., and Chi, J.T. (2015) Comprehensive profiling of amino acid response
718 uncovers unique methionine-deprived response dependent on intact creatine
719 biosynthesis. PLoS Genet. 11, e1005158. doi: 10.1371/journal.pgen.1005158.
720 65. Towbin, B.D., González-Aguilera, C., Sack, R., Gaidatzis, D., Kalck, V., Meister, P.,
721 Askjaer, P., and Gasser, S.M. (2012) Step-wise methylation of histone H3K9 positions
722 heterochromatin at the nuclear periphery. Cell. 150, 934-937.
723 66. Tvardovskiy, A., Schwämmle, V., Kempf, S.J., Rogowska-Wrzesinska, A., and Jensen,
724 O.N. (2017) Accumulation of histone variant H3.3 with age is associated with profound
725 changes in histone methylation landscape. Nucleic Acids Res. 45, 9272-9289.
726 67. Van Meter, M., Kashyap, M., Rezazadeh, S., Geneva, A.J., Morello, T.D., Seluanoc, A.,
727 and Gorbunova, V. (2014) SIRT5 represses LINE1 retrotransposons by ribosylating
728 KAP1 but this repression fails with stress and age. Nat. Commun. Article number 5011.

729 68. Wang, Z., Yip, L.Y., Lee, J.H.J., Wu, Z., Chew, H.Y., Chong, P.K.W., Teo, C.C., Ang,
730 H.Y.K., Peh, K.L.E., Yuan, J., Ma, S., Choo, L.S.K., Basri, N., Jiang, X., Yu, Q., Hillmer,
731 A.M., Lim, W.T., Lim, T.K.H., Takano, A., Tan, E.H., Tan, D.S.W., Ho, Y.S., Lim, B., and
732 Tam, W.L. (2019) Methionine is a metabolic dependency of tumor-initiating cells. Nat.
733 Med. 25, 825-837.
734 69. Watson, G.W., Wickramasekara, S., Palomera-Sanchez, Z., Black, C., Maier, C.S.,
735 Williams, D.E., Dashwood, R.H., and Ho, E. (2014) SUV39H1/H3K9me3 attenuates
736 sulforaphane-induced apoptotic signaling in PC3 prostate cancer cells. Oncogenesis. 3,
737 e131.
738 70. Wood, J.G., Hillenmeyer, S., Lawrence, C., Chang, C., Hosier, S., Lightfoot, W.,
739 Mukherjee, E., Jiang, N., Schorl, C., Brodsky, A.S., Neretti, N., and Helfand, S.L. (2010)
740 Chromatin remodeling in the aging genome of Drosophila. Aging Cell. 9, 971-978.
741 71. Wood, J.G., Jones, B.C., Jiang, N., Chang, C., Hosier, S., Wickremesinghe, P., Garcia,
742 M., Harnett, D.A., Burhenn, L., Neretti, N., and Helfand, S.L. (2016) Chromatin-modifying
743 genetic interventions surpress age-associated transposable element activation and
744 extend life span in *Drosophila*. Proc. Natl. Acad. Sci. 113, 11277-11282.
745 72. Wu, S.E., Huskey, W.P., Borchardt, R.T., and Schowen, R.L. (1983) Chiral instability at
746 the sulfur of S-adenosylmethionine. Biochemistry. 22, 2828-2832.
747 73. Ye, C., Sutter, B.M., Wang, Y., Kuang, Z., and Tu, B.P. (2017) A metabolic function for
748 phospholipid and histone methylation. Mol. Cell 66, 180-193.
749 74. Yu, D., Yang, S.E., Miller, B.R., Wisinski, J.A., Sherman, D.S., Brinkman, J.A.,
750 Tomasiewicz, J.L., Cummings, N.E., Kimple, M.E., Cryns, V.L., and Lamming, D.W.
751 (2018) Short-term methionine deprivation improves metabolic health via sexually
752 dimorphic, mTORC-1 independent mechanisms. FASEB J. 32, 3471-3482.
753 75. Zhang, Y., Liu, T., Meyer, C.A., Eeckhoute, J., Johnson, D.S., Bernstein, B.E.,
754 Nusbaum, C., Myers, R.M., Brown, M., Li, W., and Liu, X.S. (2008) Model-based
755 analysis of ChIP-Seq (MACS). Genome Biol. 9, R137. doi: 10.1186/gb-2008-9-9-r137.
756 76. Zee, B.M., Levin, R.S., Xu, B., Leroy, G., Wingreen, N.S., and Garcia, B.A. (2010) In
757 vivo residue-specific histone methylation dynamics. J. Biol. Chem. 285, 3341-3350.
758

759 **Main Figure Titles and Legends**

760

761 Figure 1. Methionine Restriction Stimulates Dynamic Histone PTM Response

762

763 (A) Metabolic pathway diagram illustrating changes in Met-cycle metabolite abundance after 24
764 hours and 5 weeks of Met-restriction in HCT116 cells and C57BL/6J liver, respectively. n=5,
765 error bars represent SD, *p<0.05 (Welch's t-Test). (*B-C*) Plots illustrating global, relative 5mC
766 DNA methylation levels during Met-restriction. n≥3, error bars represent SD, *p<0.05 (Welch's t-
767 Test) (*D-E*) Hierarchichal clustered heatmaps of LC-MS/MS generated $\log_2$ fold-change
768 stoichiometric histone H3 peptide proteoform values relative to 0-hour or chow diet controls in
769 HCT116 cells and C57BL/6J liver, respectively. n≥3, *p<0.05, **p<.01 (Welch's t-Test). See
770 also Table S1 and Figure S1.

771

772 Figure 2. Decreased SAM Availability Drives Robust Histone Methylation Response

773

774 (*A*) Pathway diagram illustrating experimental approaches to depleting intracellular SAM
775 availability. (*B*) Bar graph of relative *MAT2A* mRNA abundance in HCT116 cells as measured
776 by RT-qPCR. n≥2, error bars represent SD, *p<0.05 (Welch's t-Test). (*C-D*) Dot plots of relative
777 Met and SAM levels in HCT116 cells. n≥4, *p<0.05 (Welch's t-test). (*E-F*) Correlation plot of LC-
778 MS/MS generated $\log_2$ fold-change stoichiometric values for individual histone H3 peptide
779 proteoforms. n=3. (*G*-J) Bar graphs illustrating LC-MS/MS generated $\log_2$ fold-changes for
780 individual H3K9 PTMs. n=3 *p<0.05 (Welch's t-test) See also Table S1, Table S2, and Figure
781 S2.

782

783 Figure 3. H3K9me1 Abundance under SAM Depletion is Driven by *de novo* Methylation

784 (*A-B*) Bar graphs illustrating LC-MS/MS generated $\log_2$ fold-changes for individual H3K9 PTMs
785 in HCT116 cells. n≥2, error bars represent SD, *p<0.05 (Welch's t-Test). (*C*) Bar graph
786 illustrating percent loss in global H3K9me1, as measured by LC-MS/MS, in response to 5μm
787 UNC0642 treatment. n≥2, error bars represent SD, *p<0.05 (Welch's t-Test) (*D*) Scatter plot of
788 relative, total H3 and H3K9me1 cytoplasmic protein abundance in HCT116 cells as measured
789 by western blot. Error bars represent SD, n=3, *p<0.05 (Welch's t-Test). (*E*) Representative
790 western blot images of those used for the quantification presented in Figure 3E. Alpha-Tubulin
791 is used as a cytoplasm marker to confirm efficient sub-cellular fractionation. See Document S1
792 for REVERT Total Protein Stain images used for normalization. (*F*) Diagram illustrating the

793 SILAC experimental design. (*G*) Bar graph illustrating contribution of newly synthesized histone
794 H3 to the total chromatin bound pool after 24 hours of Met-restriction in HCT116 cells as
795 measured by LC-MS/MS. n≥2, error bars represent SD, *p<0.05 (Welch's t-test). (*H*) Bar graph
796 illustrating ratio of light:heavy L-Arg isotope presence in H3K9 proteoforms after 24 hours of
797 Met-restriction in HCT116 cells as measured by LC-MS/MS. n≥2, Error bars represent SD,
798 *p<0.05 (Welch's t-Test). (*I*) Pie chart depicting sources of H3K9me1 during SAM depletion. (*J*)
799 Scatter plot of 373 cytoplasmic proteins identified by LC-MS/MS with significant incorporation of
800 L-Arg $_{+0}$ that were also significantly upregulated after 24 hours of Met-restriction in 0.1% DMSO
801 treated HCT116 cells. n=4, Statistical significance of p<0.05 (Welch's t-Test). See also Table
802 S1, Table S3, and Figure S3.
803
804 Figure 4. H3K9me1 is Redistributed Over Repetitive and Transposable Elements During SAM
805 Depletion
806
807 (*A*-*B*) Bar graphs illustrating percent changes in H3K9 PTM peak number at various annotated
808 loci after 24 hours of Met-restriction in HCT116 cells. (*C*-*D*) Plots depicting changes in
809 normalized H3K9 PTM ChIP-sequencing reads to loci of lost H3K9me3 after 24 hours of Met-
810 restriction in HCT116 cells. (*E*) Bar graphs illustrating percent changes in loci annotation for
811 regions of lost H3K9me3 experiencing increased relative to decreased H3K9me1 ChIP read
812 enrichment after 24 hours of Met-restriction in HCT116 cells. (*F*) Representative ChIP-
813 sequencing track image.
814
815 Figure 5. *De novo* H3K9 Mono-methylation Preserves Heterochromatin Stability
816
817 (*A*) Bar graph illustrating the percent abundances of 5 distinct nucleosome species following
818 MNase digestion of HCT116 cells. n≥3, error bars represent SD, *p<0.05 (Welch's t-Test). (*B*)
819 Representative DNA agarose gel image of those used for the quantification presented in Figure
820 5A. (C-*E*) Bar graphs illustrating relative mRNA abundances of *LINE* 1, *HERV-K,* and *HERV-R*
821 in HCT116 cells as measured by RT-qPCR. n≥4, error bars represent SD, *p<0.05 (Welch's t-
822 Test). See also Table S2.
823
824 Figure 6. Adaptive H3K9 Mechanisms Support Epigenetic Persistence Upon Metabolic
825 Recovery
826

827 (*A*) Diagram illustrating the experimental design for replenishing Met and SAM availability after
828 24 hours of Met-restriction coupled with acute 5 μM UNC0642 or 0.1% DMSO treatment in
829 HCT116 cells. (*B*) Heatmap of $\log_2$ fold-change stoichiometric values for histone H3 and H4
830 peptides as measured by LC-MS/MS. n=4, *p<0.05, **p<0.01 (Welch's t-Test). (*C-E*) Bar graphs
831 illustrating $\log_2$ fold-changes for individual H3K9 PTMs in HCT116 cells as measured by LC-
832 MS/MS. n=4, error bars represent SD, *p<0.05 (Welch's t-Test). (*F*) PCA diagram of TPM
833 values. (*G*) EBseq multiple condition comparison diagram. (*H*) Pie chart illustrating percent
834 allocation of genes identified via RNA-sequencing to all EBseq patterns. (*I-J*) Scatter plots
835 illustrating NES and FDR q-value for GSEA identified GO terms. (*K-L*) Representative GSEA
836 running enrichment score figures. See also Table S1 and Figure S4.
837
838 Figure 7. Adaptive and Persistent Epigenetic Responses to SAM Depletion are Robust *in vivo,*
839 Independent of Age
840
841 (*A*) Diagram depicting the experimental design for *in vivo* Met-restriction of 6- and 22-month
842 C57BL/6J mice followed by dietary Met-reintroduction. (*B*) Heatmap of $\log_2$ fold-change
843 stoichiometric values for histone H3 and H4 peptides in C57BL/6J liver relative to age-matched
844 controls as measured by LC-MS/MS. n≥5, *p<0.05, **p<0.01 (Welch's t-Test). (*C*) Bar graph
845 illustrating $\log_2$ fold-changes for individual H3K9 PTMs in liver from Met-restricted C57BL/6J
846 mice relative to age-matched controls as measured by LC-MS/MS. n≥5, error bars represent
847 SD, *p<0.05 (Welch's t-Test). (*D-E*) Bar graphs illustrating relative mRNA abundances of *LINE*
848 *1*, *SINE B1*, and *SINE B2* in C57BL/6J liver as measured by RT-qPCR. n≥5, error bars
849 represent SD, *p<0.05 (Student's t-Test). (*F*) Bar graph illustrating $\log_2$ fold-changes for
850 individual H3K9 PTMs in liver from C57BL/6J relative to age-matched controls as measured by
851 LC-MS/MS. n≥5, error bars represent SD, *p<0.05, (Welch's t-Test). (*G-H*) Bar graphs
852 illustrating relative mRNA abundances of *LINE 1*, *SINE B1*, and *SINE B2* in C57BL/6J liver as
853 measured by RT-qPCR. n≥5, error bars represent SD, *p<0.05 (Student's t-Test). See also
854 Table S1, Table S2, and Figure S5.
855

856 **Supplemental Figure Titles and Legends**

857

858 Figure S1, Related to Figure 1

859

860 (*A-D*) Scatter plots of relative abundance values for key Met-cycle metabolites in HCT116 cells
861 as measured by LC-MS. n=5, error bars represent SD, *p<0.05 (Welch's t-Test). (*E-J*)
862 Correlation plots of LC-MS/MS generated log_2 fold-change stoichiometric values for individual
863 histone H3 peptide proteoforms. n≥3. See also Table S1.

864

865 Figure S2, Related to Figure 2

866

867 *(*A) Diagram illustrating the experimental design for determining the conservation of H3K9
868 regulation in response to SAM depletion across various biological systems. (*B-F*) Bar graphs
869 illustrating log_2 fold-changes for individual H3K9 in response to *in vitro* SAM depletion. n=3, error
870 bars represent SD, *p<0.05 (Welch's t-Test). See also Table S1.

871

872 Figure S3, Related to Figure 3

873

874 (*A-C*) Scatter plots of relative HMT mRNA abundance in HCT116 cells as measured by RT-
875 qPCR. n=4, error bars represent SD, *p<0.05 (Welch's t-Test). (*D*) Heatmap of log_2 fold-change
876 stoichiometric values for unique histone H3K9 peptide proteoforms in HCT116 cells. n=4,
877 *p<0.05 (Welch's t-Test). (*E*) Scatter plot of relative cell counts for attached HCT116 cells. n=4,
878 error bars represent SD, *p<0.05 (Welch's t-Test). (F) Bar graph of relative H3K9me1
879 abundance in HCT116 cells as measured by western blot with accompanied representative blot
880 image. See Document S1 for REVERT Total Protein Stain image used for normalization. Error
881 bars represent SD, n≥3, *p<0.05 (Welch's t-Test). (*G*) Bar graphs illustrating log_2 fold-changes
882 for individual H3K9 PTMs. n≥3, *p<0.05 (Welch's t-Test). (*H*) Bar graph showing average
883 incorporation of L-Arg_{+10} in H3K9 peptide proteoforms. n=4, error bars represent SD. (*I*) Density
884 plot illustrating the percentage of Met residue frequency in the primary amino acid sequence of
885 all identified cytoplasmic proteins as well as those determined to be preferentially translated.
886 See also Table S1, Table S2, and Table S3.

887

888 Figure S4, Related to Figure 6

889

890 (*A*) Bar graphs illustrating log_2 fold-changes for individual H3K9 PTMs 24 hours following
891 UNC0642 removal. n=4, error bars represent SD, *p<0.05 (Welch's t-Test). *(B-C)* Bar graphs
892 illustrating relative recombinant enzyme activity in the presence of saturating amounts
893 UNC0642 and following 1000x or 10,000x overnight dialysis. n=4, error bars represent SD,
894 *p<0.05 (Welch's t-Test).
895
896 Figure S5, Related to Figure 6
897
898 (*A*) GSEA heatmap of relative gene expression across positive NES GO terms for Pattern 2. (B)
899 GSEA set-to-set heatmap illustrating gene enrichment overlap across positive NES GO terms
900 for Pattern 2. (*C*) GSEA heatmap of relative gene expression across negative NES GO terms
901 for Pattern 2. (D) GSEA set-to-set heatmap illustrating gene enrichment overlap across negative
902 NES GO terms for Pattern 2.
903
904 Figure S6, Related to Figure 7
905
906 (*A-E*) Bar graphs illustrating log_2 fold-changes for individual H3K4, H3K18/K23, H3K27, H3K36,
907 and H4 PTMs in liver from Met-restricted C57BL/6J mice relative to age-matched controls as
908 measured by LC-MS/MS. n≥5, error bars represent SD, *p<0.05 (Welch's t-Test). (F) Bar graph
909 illustrating changes in fat, lean mass, and total body mass (BW) after 3 weeks of control or Met-
910 restricted diet feeding. n=14, error bars represent SEM, *p<0.05 (two-way ANOVA). (*G*)
911 Glucose tolerance test in 6- and 22-month C57BL/6J mice after 2 weeks of control or Met-
912 restricted diet feeding. n=14, error bars represent SEM, *p<0.05 (two-way ANOVA). (*H*) Bar
913 graph illustrating changes in fat, lean mass, and total body mass (BW) after 5 weeks of control
914 diet feeding following either 3 weeks of control or Met-restricted diet feeding. n≥6, error bars
915 represent SEM, *p<0.05 (two-way ANOVA). (*I*) Glucose tolerance test in 6- and 22-month
916 C57BL/6J mice after 4 weeks of control diet feeding following either 3 weeks of control or Met-
917 restricted diet feeding. n≥7, error bars represent SEM, *p<0.05 (two-way ANOVA). See also
918 Table S1 and Table S2.
919
920 **Star Methods Text**
921
922 Contact for Reagent and Resource Sharing:
923

924 Further information and requests for resources and reagents should be directed to and will be
925 fulfilled by the Lead Contact, John M. Denu (john.denu@wisc.edu).
926
927 Experimental Model and Subject Details
928
929 *Animals and Diets:*
930
931 All experiments involving animals were approved by the Institutional Animal Care and Use
932 Committee of the William S. Middleton Memorial Veterans Hospital, Madison WI. To test the
933 effect of Met deprivation in the context of young mice, 9-week-old male C57BL/6J mice were
934 purchased from The Jackson Laboratory (Bar Harbor, ME, USA) and placed on either an amino
935 acid defined Control diet (TD.01084, Envigo, Madison, WI, USA) or a Met-deficient diet
936 (TD.140119, Envigo, Madison, WI, USA) their respective diets at 14 weeks of age; full diet
937 compositions for these diets have been previously described (PMID: 29401631). After 5 weeks
938 on the diet, mice were sacrificed following an overnight fast and liver was flash frozen for
939 analysis as described.
940
941 To compare the effect of Met restriction on young and old mice, C57BL/6J. Nia male mice were
942 obtained from the National Institute on Aging Aged Rodent Colony, and housed in our animal
943 facility for 3-4 months until reaching 5 and 21 months of age. All animals were then placed on
944 the Control diet (TD.01084) for 4 weeks, until the mice were 6 and 22 months of age. Mice were
945 then randomized to either remain on the Control diet, or were placed on the Met-deficient diet
946 (TD.140119) for three weeks. Liver was collected and flash-frozen in liquid nitrogen harvested
947 from mice euthanized after an approximately 16-hour fast.
948
949 *Cell Lines:*
950
951 HCT116, HEK-293, HEK-293T, HMCF7, Panc1, HepG2, and HepA1 cell lines were cultured at
952 37$_{o}$C with 5.0% CO_2.
953
954 Method Details
955
956 *Metabolite Extraction:*
957

958 For HCT116 cells, ~1.5x10^6 cells were quickly rinsed 3 times with 1.5 ml ice-cold PBS pH 7.4
959 before the addition of 1.5 ml of -80$_o$C 80:20 MeOH:H_2O extraction solvent. Cells were incubated
960 with extraction solvent at -80$_o$C for 15 minutes. Next, cells were scraped off their dish and
961 transferred into a 2 ml microcentrifuge Eppendorf tube which was followed by a 5-minute,
962 maximum speed centrifugation at 4$_o$C. The supernatant was transferred to a new 2 ml
963 microcentrifuge Eppendorf tube. Next, 0.5 ml extraction solvent was added to the remaining
964 pellet, vortexed, and again centrifugated at maximum speed for 5 minutes at 4$_o$C. The 2
965 supernatants from each extraction were pooled and dried completely using a Thermo Fisher
966 Savant ISS110 SpeedVac. Dried metabolite extracts were resuspended in 80 μl of 85%
967 acetonitrile following microcentrifugation for 5 minutes at maximum speed at 4$_o$C to pellet any
968 remaining insoluble debris. The supernatant was then transferred to a glass vial for LC-MS
969 analysis.
970
971 For *M. musculus* liver tissue, an average tissue weight of 75 mg was powdered in liquid nitrogen
972 using a mortar and pestle. Powdered tissue was transferred to an individual 1.5 ml
973 microcentrifuge Eppendorf tube and incubated with 1 ml -80$_o$C 80:20 MeOH:H_2O extraction
974 solvent on dry ice for 5 minutes post-vortexing. Tissue homogenate was centrifugated at
975 maximum speed for 5 minutes at 4$_o$C. Supernatant was transferred to a 15 ml tube after which
976 the remaining pellet was resuspended in 0.8 ml -20$_o$C 40:40:20 ACN:MeOH:H_2O extraction
977 solvent and incubated on ice for 5 minutes. Tissue homogenate was again centrifugated at
978 maximum speed for 5 minutes at 4$_o$C after which the supernatant was pooled with the
979 previously isolated metabolite fraction. The 40:40:20 ACN:MeOH:H_2O extraction was then
980 repeated as previously described. Next, 550 μl of pooled metabolite extract for each sample
981 was transferred to a 1.5 ml microcentrifuge Eppendorf tube and completely dried using a
982 Thermo Fisher Savant ISS110 SpeedVac. Dried metabolite extracts were resuspended in 450 μl
983 of 85% ACN following microcentrifugation for 5 minutes at maximum speed at 4$_o$C to pellet any
984 remaining insoluble debris. Supernatant was then transferred to a glass vial for LC-MS analysis.
985
986 *LC-MS Metabolite Analysis:*
987
988 Each prepared metabolite sample was injected onto a Thermo Fisher Scientific Vanquish
989 UHPLC with a Waters XBridge BEH Amide column (100 m x 2.1 mm, 3.5 μm) coupled to a
990 Thermo Fisher Q-Exactive mass spectrometer. Mobile phase (A) consisted of 97% H_2O, 3%
991 ACN, 20 mM ammonium acetate, and 15 mM ammonium hydroxide pH 9.6. Organic phase (B)

992 consisted of 100% ACN. Metabolites were resolved using the following linear gradient: 0 min,
993 85% B, 0.15 ml/min; 1.5 min, 85% B, 0.15 ml/min; 5.5 min, 40% B, 0.15 ml/min; 10 min, 40% B,
994 0.15 ml/min; 10.5 min, 40% B, 0.3 ml/min; 14.5 min, 40% B, 0.3 ml/min; 15 min, 85% B, 0.15
995 ml/min; 20 min, 85% B, 0.15 ml/min. The mass spectrometer was operated in positive ionization
996 mode with a MS1 scan at resolution = 70,000, automatic gain control target = 3 x 10_6, and scan
997 range = 60-186 m/z and 187-900 m/z. This protocol was adapted from Mentch et al., 2015.
998 Individual metabolite data were called using MAVEN (Melamud et al., 2010; Clasquin et al.,
999 2012) with retention times empirically determined in-house. Peak Area Top values were
1000 analyzed to determine metabolite expression.
1001
1002 *LC-MS DNA Methylation Assay:*
1003
1004 500 ng of cytosine, 5mC, and 5hmC double-stranded DNA standards from Zymo Research
1005 were incubated with Zymo Research DNA Degradase Plus for 3 hours at 37$_o$C following enzyme
1006 inactivation at 70$_o$C for 20 minutes. 75 μl of ACN was added to each standard reaction to bring
1007 the final volume to 100 μl. DNA standards were centrifugated at 21,100xg for 5 minutes at 4$_o$C
1008 after which 75 μl of supernatant was transferred to a glass vial for LC-MS analysis. A range of
1009 0.1 to 100 ng of digested DNA was analyzed via LC-MS to determine each nucleoside's linear
1010 range of detection.
1011
1012 Genomic DNA extracted using a Promega Wizard Genomic DNA Purification Kit after which 1
1013 μg was incubated with Zymo Research DNA Degradase Plus at 37$_o$C following enzyme
1014 inactivation at 70$_o$C for 20 minutes. 175 μl of ACN was added to each reaction to bring the final
1015 volume to 200 μl. DNA samples were centrifugated at 21,100xg for 5 minutes at 4$_o$C after which
1016 150 μl of supernatant was transferred to a glass vial for LC-MS analysis.
1017
1018 Each prepared nucleoside sample was injected onto a Thermo Fisher Scientific Vanquish
1019 UHPLC with a Waters XBridge BEH Amide column (100 m x 2.1 mm, 3.5 μm) coupled to a
1020 Thermo Fisher Q-Exactive mass spectrometer run in positive ionization mode. Mobile phase (B)
1021 consisted of H_2O, 3% ACN, 20 mM ammonium acetate, and 15 mM ammonium hydroxide pH
1022 9.6. Organic phase (B) consisted of 100% ACN. Nucleosides were resolved using the following
1023 linear gradient: 0 min, 85% B, 0.15 ml/min; 1.5 min, 85% B, 0.15 ml/min; 5.5 min, 40% B, 0.15
1024 ml/min; 10 min, 40% B, 0.15 ml/min; 10.5 min, 40% B, 0.3 ml/min; 14.5 min, 40% B, 0.3 ml/min;

1025 15 min, 85% B, 0.15 ml/min; 20 min, 85% B, 0.15 ml/min. The mass spectrometer was operated
1026 in positive ionization mode with a MS1 scan at resolution = 70,000, automatic gain control target
1027 = 3 x 10_6, and scan range = 200-300 m/z, followed by a DDA scan with a loop count of 5. DDA
1028 settings were as follows: window size = 2.0 m/z, resolution = 17,500, automatic gain control
1029 target = 1 x 10_5, DDA maximum fill time = 50 ms, and normalized collision energy = 30. This
1030 protocol was adapted from Mentch et al., 2015. Individual metabolite data were called using
1031 MAVEN (Melamud et al., 2010; Clasquin et al., 2012) with retention times empirically
1032 determined in-house. Peak Area Top values were analyzed to determine metabolite expression
1033 with dAdenosine being utilized for internal normalization (m/z dCytosine: 228.0978, m/z d5mC:
1034 242.1135, m/z d5hmC: 258.108, m/z dAdenosine: 252.109).
1035
1036 *Histone Isolation and Chemical Derivatization:*
1037
1038 Tissue culture cell pellets were resuspended in 800 μl of ice-cold Buffer A (10 mM Tris-HCl pH
1039 7.4, 10 mM NaCl, and 3 mM $MgCl_2$) supplied with protease and histone deacetylase inhibitors
1040 (10 μg/ml leupeptin, 10 μg/ml aprotinin, 100 μM phenylmethylsulfonyl fluoride, 10 mM
1041 nicotinamide, 1 mM sodium-butyrate, and 4 μM trichostatin A) followed by 80 strokes of light
1042 pestle homogenization in a 1 ml Wheaton dounce homogenizer. Cell homogenate was then
1043 transferred to a 1.5 ml microcentrifuge Eppendorf tube and centrifugated at 800xg for 10
1044 minutes at 4_oC to pellet nuclei. The supernatant was either transferred to a fresh 1.5 ml
1045 Eppendorf tube or discarded. The nuclei pellet was resuspended in 500 μl ice-cold PBS pH 7.4
1046 followed by centrifugation at 800xg for 10 minutes at 4_oC. The supernatant was discarded and
1047 nuclei were again washed with 500 μl ice-cold PBS pH 7.4. Pelleted nuclei were then
1048 resuspended in 500 μl of 0.4N H_2SO_4 and rotated at 4_oC for 4 hours. Samples were
1049 centrifugated at 3,400xg for 5 minutes at 4_oC to pellet nuclear debris and precipitated non-
1050 histone proteins. The supernatant was transferred to a new 1.5 ml Eppendorf tube after which
1051 125 μl of 100% trichloroacetic acid was added and incubated overnight on ice at 4_oC. Samples
1052 were centrifugated at 3,400xg for 5 minutes at 4_oC to pellet precipitated histone proteins. The
1053 supernatant was discarded, after which the precipitant was washed with 1 ml ice-cold acetone
1054 +0.1% HCl. Samples were centrifugated at 3,400xg for 2 minutes at 4_oC and the supernatant
1055 was discarded. This process was repeated except precipitant was washed with 100% ice-cold
1056 acetone. Residual acetone was allowed to evaporate at room temperature for 10 minutes after
1057 which the dried precipitant was dissolved in 125 μl H_2O. Samples were then centrifugated at

1058 21,100xg for 5 minutes at 4$_o$C to pellet any remaining insoluble debris. Supernatant containing
1059 purified histone was then transferred to a new 1.5 ml Eppendorf tube and stored at -20$_o$C until
1060 needed for future analyses.
1061
1062 For *M. musculus* liver tissue, an average tissue weight of 50 mg was homogenized in 800μl ice-
1063 cold Buffer supplemented with protease and HDAC inhibitors (listed above) using a 1 ml
1064 Wheaton dounce homogenizer (20 strokes of the loose pestle followed by 20 strokes of the tight
1065 pestle) and strained through a 100 μM filter before being transferred to a new 1.5 ml Eppendorf
1066 tube. All remaining steps for completing the histone isolation were performed as described
1067 previously in the tissue culture isolation protocol.
1068
1069 To prepare purified histone proteins for LC-MS/MS analysis, 5 μg of histone was diluted with
1070 H_2O to a final volume of 9 μl. 1 μl of 1 M triethylammonium bicarbonate was added to each
1071 sample to buffer the solution to a final pH of 7-9. Next, 1 μl of 1:100 propionic anhydride:H_2O
1072 was added to each sample and allowed to incubate for 2 minutes at room temperature. The
1073 propionylation reaction was then quenched via the addition of 1 μl 80 mM hydroxylamine which
1074 was allowed to incubate for 20 minutes at room temperature. Next, propionylated histones were
1075 digested with 0.1 μg trypsin for 4 hours at 37$_o$C. Upon completion of trypsin digestion, 5 μl of .02
1076 M NaOH was added to bring the final pH between 9-10. Propionylated, trypsin digested histone
1077 peptides were then N-terminally modified with 1 μl 1:50 phenyl isocyanate:ACN for 1-hour at
1078 37$_o$C. Modified peptides were desalted and eluted-off of Empore™C18 extraction membrane.
1079 Eluted samples were dried completely using a Thermo Fisher Scientific Savant ISS110
1080 SpeedVac, resuspended in 40 μl sample diluent (94.9% H_2O, 5% ACN, .1% TFA), and
1081 transferred into glass vials for LC-MS/MS analysis.
1082
1083 *Histone Proteomics Analysis:*
1084
1085 Derivatized histone peptides were injected onto a Dionex Ultimate3000 nanoflow HPLC with a
1086 Waters nanoEase UPLC C18 column (100 m x 150 mm, 3μm) coupled to a Thermo Fisher Q-
1087 Exactive mass spectrometer at 700 nL/ min. Aqueous phase (A) consisted of H_2O + 0.1% formic
1088 acid while the mobile phase (B) consisted of acetonitrile + 0.1% formic acid (B). Histone
1089 peptides were resolved using the following linear gradient: 0 min, 2.0% B; 5 min, 2.0% B; 65
1090 min, 35% B; 67 min, 95% B; 77 min, 95% B; 79 min, 2.0% B; 89 min, 2.0% B. Data was

1091 acquired using data-independent acquisition (DIA) mode. The mass spectrometer was operated
1092 with a MS1 scan at resolution = 35,000, automatic gain control target = 1 x 10_6, and scan range
1093 = 390-910 m/z, followed by a DIA scan with a loop count of 10. DIA settings were as follows:
1094 window size = 10 m/z, resolution = 17,500, automatic gain control target = 1 x 10_6, DIA
1095 maximum fill time = AUTO, and normalized collision energy = 30.
1096
1097 DIA Thermo .raw files were imported into Skyline open source proteomics software (MacLean et
1098 al., 2010) and matched against a pre-constructed peptide database containing unique peptide
1099 proteoforms from H3 and H4. The identity of each individually called peak was verified by hand
1100 after which total MS1 peak area values were exported for downstream analyses. To control for
1101 differences in ionization efficiencies across histone peptides, all peptides possessing an
1102 identical primary sequence were analyzed as a peptide family which enabled the calculation of
1103 stoichiometric values for each unique peptide proteoform within the family. Stoichiometric values
1104 were compared across conditions to identify altered histone peptide abundances. Furthermore,
1105 combinatorial peptide stoichiometry values were deconvoluted by totaling the stoichiometry
1106 values for all peptides possessing a given PTM independent of any other PTMs that may be
1107 present on other residues of the same primary peptide. A Welch's T-Test with a p-value cutoff of
1108 0.05 was used to determine statistical significance.
1109
1110 Hierarchical clustering was performed in MATLAB R2016a using the 'clustergram' command.
1111 Pearson's Correlation Coefficients were calculated in MATLAB R2016a using the 'corr'
1112 command.
1113
1114 *RNAi Mediated Inhibition of MAT2A and H3K9 HMT Expression:*
1115
1116 For 35 mm tissue culture dishes, 1.5x10_5 HCT116 cells were reverse transfected with 30 pmol
1117 of targeted or control RNAi using 5 μl of Lipofectamine RNAiMAX in addition to 500 μl Opti-
1118 MEM and 2.5 ml RPMI-1640 +10% FBS. MAT2A-RNAi treated HCT116 cells used for LC-MS
1119 metabolite analysis were cultured using dialyzed FBS.
1120
1121
1122 *Methionine Restriction of Tissue Culture Cells:*
1123

1124 All tissue culture cells were initially cultured in RPMI-1640 +10% FBS at 37$_o$C, 5% CO_2. One
1125 day before Met-restriction, 3.5x10$_6$ cells were seeded into 100 mm tissue culture dishes. One-
1126 hour before the restriction began, RPMI-1640 was replaced with fresh, Met replete media. At the
1127 time of Met-restriction, cells were rinsed 2x with 3 ml of sterile PBS pH 7.4 followed by addition
1128 of RPMI-1640 void of Met. Any small molecule inhibitors or vehicle controls would be added at
1129 this time.
1130
1131 For experiments in which Met-restriction was followed by Met repletion, HCT116 cells were
1132 washed with PBS pH 7.4 2x to maximize small molecule inhibitor and DMSO removal before
1133 reintroduction of Met replete RPMI-1640.
1134
1135 HCT116 cells cultured for LC-MS metabolite analysis were cultured in RPMI-1640 containing
1136 10% dialyzed FBS beginning 1-hour prior to beginning Met-restriction.
1137
1138 *SILAC in Tissue Culture:*
1139
1140 197 ml of SILAC RPMI-1640 +10% DFBS void of L-Arg and L-Lys was supplemented with 50mg
1141 isotopically heavy $3C_6$ $15N_4$ L-Arg HCl and 9.43mg isotopically light L-Lys to obtain final
1142 concentrations of 1.149 mM and 0.219 mM, respectively. HCT116 cells were cultured in the
1143 SILAC media for 7 days (or 9 doubling cycles at a reported doubling time of 21 hours) after
1144 which cells were washed 3x with 5 ml PBS pH 7.4 before replacing the SILAC media with
1145 isotopically light L-Arg and L-Lys RPMI-1640 +10% DFBS void of Met. Half of the cells were
1146 treated with 5 μM UNC0642 or 0.1% DMSO at this time. Furthermore, 0-hour control HCT116
1147 cells which were never exposed to isotopically light L-Arg, Met-restricted RPMI-1640 were
1148 harvested. HCT116 cells cultured in the Met-restricted media were harvested after 24 hours.
1149
1150 *SILAC Shotgun Proteomics Analysis:*
1151
1152 50 μg of cytoplasmic protein extract from the previously described SILAC Met-restriction
1153 experiment were diluted with H_2O into a final volume of 75 μl. Next, dithiothreitol was added to
1154 each sample at a final concentration of 10 mM, followed by a 15-minute incubation at 95$_o$C. A
1155 sonication water bath was used to resolubilize precipitated proteins post-heat denaturation.
1156 Iodoacetamide was then added to a final concentration of 20 mM, followed by a 20-minute
1157 incubation at room temperature protected from light. Alkylated proteins were precipitated with

1158 337 μl ice-cold acetone for 20 minutes at -20$_o$C. Samples were centrifugated at 21,000xg for 15
1159 minutes at 4$_o$C, the supernatant was discarded, and precipitated protein was resuspended in
1160 400 μl of urea buffer (2 M urea and 100 mM ammonium bicarbonate pH 8). Precipitated proteins
1161 were again solubilized using a sonication water bath. Solubilized proteins were digested into
1162 peptides using 0.8 μg trypsin at 37$_o$C overnight. Upon digest completion, samples were desalted
1163 and eluted-off Empore™C18 extraction membrane. Eluted samples were dried completely using
1164 a Thermo Fisher Scientific Savant ISS110 SpeedVac, after which being resuspended in 50 μl
1165 sample diluent (94.9% H_2O, 5% ACN, .1% TFA) and transferred to glass vials for LC-MS/MS
1166 analysis.
1167
1168 Each prepared cytoplasmic peptide sample was injected onto a Dionex Ultimate3000 nanoflow
1169 HPLC with a Waters nanoEase UPLC C18 column (100 m x 150 mm, 3μm) coupled to a
1170 Thermo Fisher Q-Exactive mass spectrometer at 800 nL/ min. Aqueous phase (A) consisted of
1171 H_2O + 0.1% formic acid while the mobile phase (B) consisted of acetonitrile + 0.1% formic acid
1172 (B). Histone peptides were resolved using the following linear gradient: 0 min, 5.0% B; 5 min,
1173 5.0% B; 120 min, 30% B; 122 min, 95% B; 127 min, 95% B; 129 min, 5.0% B; 145 min, 5.0% B.
1174 Data was acquired using data-dependent acquisition (DDA) mode. The mass spectrometer was
1175 operated with a MS1 scan at resolution = 70,000, automatic gain control target = 1 x 10_6, and
1176 scan range = 400-1000 m/z, followed by a DDA scan with a loop count of 20. DDA settings were
1177 as follows: window size = 2.0 m/z, resolution = 17,500, automatic gain control target = 2 x 10_5,
1178 DDA maximum fill time = 150 ms, and normalized collision energy = 28.
1179
1180 *MaxQuant Proteomics Analysis:*
1181
1182 Thermo .raw DDA files were analyzed using MaxQuant v1.6.2.6 (Cox et al., 2014) using the
1183 default settings with the following exceptions: Labels: 1, Arg10; Instrument: Orbitrap; LFQ: LFQ
1184 min. ratio count: 2, LFQ min. number of neighbors: 3, LFQ average number of neighbors: 6;
1185 FASTQ File: Proteome: *H. Sapiens* Proteome ID UP000005640.
1186
1187 Identified proteins with a Q-value of 0.01 or above were removed. For the remaining proteins,
1188 LFQ light (L-Arg$_{+0}$) and heavy (L-Arg$_{+10}$) values were summed to generate LFQ total protein
1189 abundance values. LFQ light values were divided by the corresponding LFQ total value to
1190 generate a percent abundance of LFQ light species for each identified protein. Welch's t-Tests
1191 with a p-value cut off of 0.05 were used to determine significant accumulation of LFQ light

1192 species in Met-restricted HCT116 samples relative to 0-hour controls. For proteins determined
1193 to have significant LFQ light species abundance after Met-restriction, LFQ total values were
1194 used to determine the corresponding change in overall protein abundance. Up to 2 null-values
1195 were removed from replicates of an experimental group to account for missed identifications. If
1196 3 of the 4 replicates for a single experimental group contained null-values, that protein was
1197 removed from all experiment groups and therefore excluded from any downstream analyses. A
1198 Welch's t-Test with a p-value cut off of 0.05 was used to determine if an identified protein was
1199 significantly more abundant after Met-restriction relative to 0-hour controls.
1200
1201 *SILAC Histone Proteomics Analysis:*
1202
1203 Histones were isolated, chemically derivatized, and analyzed by LC-MS/MS as described in
1204 "Histone Isolation and Chemical Derivatization" and "Histone Proteomics Analysis." DDA
1205 Thermo .raw files of histone proteins with incorporated isotopically heavy $3C_6$ $15N_4$ L-Arg were
1206 used to construct an H3K9/K14 peptide library using Skyline opensource proteomics software
1207 (MacLean et al., 2010). DIA files were then matched against both isotopically heavy and light L-
1208 Arg peptide libraries after which peptide identities were confirmed by hand. MS1 intensity values
1209 for both isotopically heavy and light L-Arg peptides were summed to generate total MS1 peptide
1210 proteoform intensity values which were then used to calculate the percent of total MS1 peptide
1211 proteoform signal which was contributed by isotopically heavy peptide proteoforms. Welch's T-
1212 Tests with a p-value cutoff of 0.05 were used to determine significant differences in total MS1
1213 peptide proteoform stoichiometric values as well as the percent contribution of isotopically
1214 heavy peptide proteoforms to total peptide proteoform intensity values.
1215
1216 *Chromatin Immunoprecipitation and Sequencing:*
1217
1218 $30x10_6$ HCT116 cells were resuspended in 1 ml MNase digestion buffer (50 mM Tris-HCl pH
1219 7.6, 1 mM $CaCl_2$, and 0.2% Triton X-100) after which 330 μl of the cell suspension was
1220 aliquoted into individual 1.5 ml tubes. Each tube was treated with either 45, 52.5, or 60 units of
1221 Worthington MNase for 5 minutes at 37$_o$C shaking at 400 rpm to generate mono-nucleosomes.
1222 MNase digestions were stopped via the addition of EDTA to a final concentration of 5mM.
1223 Digested cells were then pooled and lysed at 4$_o$C using a Covaris S220 Focused-ultrasonicator
1224 with the following settings: Peak Power = 75, Duty Factor = 5, Cycles/Burst = 100, Duration =
1225 30" on/30" off x2. Insoluble debris was centrifugated at 10,000 rpm for 10 minutes at 4$_o$C after

1226 which the supernatant containing prepared nucleosomes was transferred to a new tube.
1227 Glycerol was added to a final concentration of 5% prior to -80$_o$C storage. For input controls, 43
1228 μl of prepared nucleosomes were aliquoted and saved for further processing at -80$_o$C.
1229
1230 Next, 860 μl of prepared nucleosomes was incubated with 5 μg of the desired antibody, rotating
1231 overnight at 4$_o$C. The nucleosome/antibody solution was added to 50 μl of prepared M-280
1232 Sheep Anti-Rabbit IgG superparamagnetic Dynabeads™ and allowed to rotate at 4$_o$C for 4
1233 hours. Conjugated beads were then washed for 10 minutes, rotating at 4$_o$C under the following
1234 conditions: 3x 1 ml RIPA (10 mM Tris pH 7.6, 1 mM EDTA, 0.1% SDS, 0.1% Na-deoxycholate,
1235 1% Triton X-100) buffer, 2x 1 ml RIPA buffer +0.3 M NaCl, 2x 1 ml LiCl buffer (0.25 M LiCl,
1236 0.5% NP-40, 0.5% Na-deoxycholate), 1x with 1 ml 1xTE +50 mM NaCl. Following the final
1237 wash, beads were centrifugated at 4$_o$C for 3 minutes at 960xg after which the supernatant was
1238 carefully removed and discarded.
1239
1240 To elute immunoprecipitated nucleosome species, beads were resuspended in 210 μl of elution
1241 buffer (50 mM Tris-HCl pH 8.0, 10 mM EDTA, 1% SDS) and incubated at 65$_o$C for 30 minutes
1242 shaking at 400 rpm. Beads were resuspended every 2 minutes via brief vortexing. Next samples
1243 were centrifugated at 16,000xg for 1 minute at room temperature after which 200 μl of
1244 supernatant was transferred to a new 1.5 ml Eppendorf tube. Eluted nucleosome species were
1245 then treated with 2 μl Thermo Fisher Scientific Proteinase K for 2 hours at 55$_o$C. DNA was
1246 recovered from the Proteinase K digestion using the QIAquick PCR Purification Kit.
1247
1248 DNA libraries were prepared by the University of Wisconsin-Madison Biotechnology Center
1249 using the Illumina TruSeq DNA Nano kit and then sequenced across 4 lanes of an Illumina
1250 1x100 HiSeq2500 High Throughput flowcell.
1251
1252 FASTQ files were aligned unpaired using bowtie2-2.1.0 (Langmead and Salzberg, 2012)
1253 against human genome 19. Bowtie2 output SAM files were converted to BAM files, sorted and
1254 indexed using samtools 1.5 (Li et al., 2009). Broad peaks were called from sorted BAM files
1255 using MACS2-2.1.1.20160309 (Zhang et al., 2008) with a Q-value cutoff of 0.1. Input DNA was
1256 used as the control file. All identified peaks possessing a $\log_2$ fold-change below 1.75 were
1257 discarded prior to downstream analyses. Bedtools v2.25.0 (Quinlan and Hall, 2010) was used to
1258 identify unique and overlapping across samples and also used to assign raw mapped reads to

1259 pre-specified genomic loci. Genomic loci were annotated using HOMERv4.9 (Heinz et al.,
1260 2010).
1261
1262 *Quantitative PCR:*
1263
1264 RNA was extracted from HCT116 cells using Thermo Fisher Scientific TRIzol and from liver
1265 tissue using Sigma TRI Reagent, both by following the manufacturer's instructions. The
1266 concentration and purity of RNA were determined by absorbance at 260/280 nm.
1267
1268 cDNA was prepared from 1 μg of RNA using RevertAid Reverse Transcriptase for HCT116 RNA
1269 and Superscipt III for liver RNA. Oligo dT primers were used in both cDNA synthesizing
1270 reactions.
1271
1272 HCT116 cDNA was analyzed on a Roche 480 Light Cycler System with PerfeCTa SYBR Green
1273 SuperMix while cDNA generated from liver was analyzed on an Applied Biosystems StepOne
1274 Plus instrument with Sybr Green PCR Master Mix. HCT116 cDNA qPCR reactions were
1275 normalized internally using GAPDH while liver cDNA qPCR reactions were normalized internally
1276 using actin. Primer sequences are available in Table S3.
1277
1278 *RNA sequencing*
1279
1280 RNA libraries were prepared by Novogene using NEBNext adaptors followed by paired end
1281 2x150 sequencing on their Illumina Platform. FASTQ files were trimmed using Trimmomatic
1282 v0.39 (Bolger et al., 2014) and aligned using RSEM v1.2.4 (Li et al., 2011) against the human
1283 genome 18 reference transcriptome. RSEM .genes output files were used for Ebseq
1284 EBMultiTest multiple comparison analysis (Leng et al., 2013). Gene lists associated with
1285 individual EBMultiTest patterns were further analyzed with GSEA 2 (Tamayo et al., 2005;
1286 Mootha et al., 2003)
1287
1288 *MNase Accessibility Assay:*
1289
1290 $6x10_6$ HCT116 cells were resuspended in 1 ml of digestion buffer (50 mM Tris-HCl pH 7.6, 1
1291 mM $CaCl_2$, and 0.2% Triton X-100) in addition to 15 unites of Worthington MNase. MNase
1292 treated cell suspensions were incubated for 5 minutes at 37$_o$C shaking at 400 rpm. MNase

1293 digestions were stopped via the addition of EDTA to a final concentration of 5 mM. Digested
1294 cells were then pooled and lysed at 4$_o$C using a Covaris® S220 Focused-ultrasonicator with the
1295 following settings: Peak Power = 75, Duty Factor = 5, Cycles/Burst = 100, Duration = 30" on/30"
1296 off x2. Insoluble debris was pelleted via centrifugation at 10,000 rpm for 10 minutes at 4$_o$C after
1297 which the supernatant was transferred to a new tube. 150 μl of digested chromatin was treated
1298 with 2 μl of Thermo Fisher Scientific Proteinase K for 90 minutes at 55$_o$C. DNA was then
1299 purified using the QIAquick PCR Purification Kit. Next, 1 μg of purified DNA was separated on a
1300 2% agarose gel and quantified using GelAnalyzer 2010a.
1301
1302 *Western-Blotting and Image Quantification:*
1303
1304 Protein separated on SDS-PAGE gels were transferred onto 0.2 μm nitrocellulose membrane
1305 and stained with 5 ml of LI-COR REVERT Total Protein Stain for 5 minutes at room temperature
1306 before being blocked in 0.1% fat-free milk PBS pH 7.4 for 1 hour. Primary antibodies were
1307 diluted 1:1000 in 5% fat-free milk PBST pH 7.4 and incubated with the membrane overnight at
1308 4$_o$C. LI-COR secondary antibodies were used at a 1:15,000 dilution in 5% fat-free milk PBST pH
1309 7.4 and incubated with the membrane for 1 hour at room temperature. Membranes were imaged
1310 using an Odyssey Infrared Imager (model no. 9120). Densitometry was performed using Image
1311 Studio™ Lite software. All data was normalized to REVERT™ Total Protein Stain.
1312
1313 *In vivo Tests:*
1314
1315 For glucose tolerance tests, mice were fasted overnight for 16 hours and then injected with
1316 glucose (1 g/kg) intraperitoneally as previously described (Arriola Apelo et al., 2016). Glucose
1317 measurements were taken using a Bayer Contour blood glucose meter and test strips. Mouse
1318 body composition was determined using an EchoMRI Body Composition Analyzer (EchoMRI$_{TM}$,
1319 Houston, TX, USA) according to the manufacturer's procedures.
1320
1321 *Protein Purification:*
1322
1323 The *H. sapiens* Ehmt1 catalytic subunit *E. coli* expression plasmid used in this study (Addgene
1324 plasmid # 51314) was acquired from addgene, made possible through a gift by Cheryl
1325 Arrowsmith. The *H. sapiens* Ehmt2 catalytic subunit *E. coli* expression plasmid used in this
1326 study was provided by the laboratory of Peter W. Lewis at the University of Wisconsin-Madison.

1327

1328 Transformed Rosetta™ *E. coli* competent cells were cultured in 1L of 2XYT media at 37$_o$C to an
1329 O.D. 600 of 0.8. IPTG was then added to each culture at a final concentration of 1mM. Cultures
1330 were allowed to grow for 16 hours at 18$_o$C before being harvested and stored at -80$_o$C. Pellets
1331 were resuspended in 30ml Buffer A (50 mM NaPi, 250 mM NaCl, 10mM imidazole, pH 7.2) and
1332 lysed using sonicated in the presence of lysozyme. Lysate was centrifugated and the
1333 supernatant was collected. The supernatant was then loaded onto a HisTrap FF nickel column
1334 in line with a GE AKTA FPLC. Protein was eluted off the column using a linear gradient ending
1335 in 100% Buffer B (50 mM NaPi, 250 mM NaCl, 250 mM imidazole, pH 7.2) and collected into
1336 time-dependent fractions. Fractions were analyzed by coomassie staining of SDS-PAGE gels to
1337 assess purity.

1338

1339 *Histone Methyltransferase Activity Assay:*

1340

1341 The methyltransferase activity of recombinantly purified Ehmt1 and Ehmt2 catalytic subunits
1342 was assessed using Promega Corporation's MTase-Glo™ Methyltransferase Assay. Assays
1343 were performed using 12.5 nM enzyme in the presence of saturating concentrations of SAM (30
1344 μM) and unmodified H3K9 peptide (30 μM, WARTKQTARKSTGGKAPR – 3') as well as either
1345 saturating levels of UNC0642 (5 μM) or 0.1% DMSO. Reactions proceeded for 1 hour at 30$_o$C
1346 before addition of MTase-Glo™ reagent following the Promega protocol. Luminescence was
1347 detected using a Biotek Synergy H4 Hybrid plate reader. All values detected were determined to
1348 be within the instrument's linear range of detection via the use of a SAH standard curve. To test
1349 for reversibility of enzyme inhibition by small molecule, 1 μM Ehmt1 and Ehmt2 were incubated
1350 with saturating concentrations of UNC0642 (5 μM) or 0.1% DMSO followed overnight 1,000x or
1351 10,000x dialysis with a molecular weight cutoff of 10,000 Da against 1x Reaction Buffer without
1352 BSA (20mM Tris, pH 8.0, 50mM NaCl, 1mM EDTA, 3mM $MgCl_2$, 1mM DTT). Following dialysis,
1353 enzyme and reaction components were diluted using the appropriate dialysis buffers to the
1354 working concentrations described above. The MTase-Glo™ assay was then repeated using
1355 identical conditions as described above.

1356

1357 *Quantification and Statistical Analysis*

1358

1359 Explanations of statistical analyses and parameters are present in the main and supplemental
1360 figure legends as well as in 'Method Details" where appropriate.

1361

1362 *Data and Software Availability*

1363

1364 RNA-sequencing as well as H3K9me1 and H3K9me3 ChIP-sequencing data have been
1365 uploaded to Gene Expression Omnibus (GEO) and will be made publicly available upon
1366 manuscript publication.

1367

1368 **KEY RESOURCES TABLE**

1369

REAGENT or RESOURCE	SOURCE	IDENTIFIER
Antibodies		
Rabbit polyclonal anti-H3K9me1	Abcam	Cat#ab176880; RRID#AB_2751009
Rabbit polyclonal anti-H3K9me3	Abcam	Cat#ab8898; RRID#AB_306848
Rabbit polyclonal anti-Histone H3	Abcam	Cat#ab46765; RRID#AB_880439
Rabbit monoclonal anti-alpha Tubulin	Cell Signaling Technologies	Cat#cst2125; RRID#AB_2619646
IRDye® 800CW Goat anti-Rabbit	LI-COR Biosciences	Cat#925-32211; RRID#AB_2651127
Chemicals, Peptides, and Recombinant Proteins		
UNC0642 G9a/GLP Inhibitor	R&D Systems	Cat#5132/10
DNA Degradase Plus	Zymo Research	Cat#E2020
Lipofectamine RNAiMax	Thermo Fisher	Cat#13778030
L-Lysine-2HCl	Thermo Fisher Scientific	Cat#PI89987
L-Arginine-HCl 13C6 15N4	Thermo Fisher	Cat#PI89990
Dimethyl Sulfoxide (DMSO)	Sant Cruz Biotechnology	Cat#sc-358801
Sequencing Grade Modified Trypsin	Promega	Cat#V5113
Propionic Anhydride	Sigma-Aldrich	Cat#240311
Phenyl Isocyanate	Sigma-Aldrich	Cat#78750-25ML
Leupeptin Hemisulfate	Thermo Fisher	Cat#AAJ61188MC
Aprotinin	Gold Biotechnology	Cat#A-655-100
Phenylmethylsulfonyl Fluoride (PMSF)	Gold Biotechnology	Cat#P-470-50
Trichostatin A	Thermo Fisher	Cat#501012404
Sodium Butyrate	Sigma-Aldrich	Cat#303410-100G
Nicotinamide	Sigma-Aldrich	Cat#N3376-500G
Urea	Acros Organics	Cat#197460050
Dithiothreitol (DTT)	Gold Biotechnology	Cat#DTT100
Iodoacetamide	Sigma-Aldrich	Cat#I1149-5G

Ammonium Bicarbonate	Sigma-Aldrich	Cat#09830-500G
Micrococcal Nuclease (MNase)	Worthington Biochemical	Cat#LS004798
Proteinase K	Thermo Fisher	Cat#EO0491
TRIzol™	Thermo Fisher	Cat#15596018
TRI Reagent	Sigma-Aldrich	Cat#T9424-25ML
3M Empore C18 47mm extraction disks	Empore	Cat#2215
Atlantis dC18 NanoEase Column (3 μM, 100 μM, 150 mm)	Waters	Cat#186002209
XBridge BEH Amide Column (3.5 μM, 2.1 mm, 150mm)	Waters	Cat#186004860
Superscript III Reverse Transcriptase	Thermo Fisher	Cat#18080044
RPMI-1640	Thermo Fisher	Cat#11875119
RPMI-1640 for SILAC	Thermo Fisher	Cat#88365
RPMI-1640, no methionine	Thermo Fisher	Cat#A1451701
Fetal Bovine Serum (FBS)	Thermo Fisher	Cat#16000044
Dialyzed Fetal Bovine Serum (DFBS)	Thermo Fisher	Cat#88212
H3K9 unmodified peptide	This paper	N/A
pET28a-LIC-4H4H	Addgene	Plasmid # 51314; RRID#Addgene_51314
pET28a-LIC-EHMT2-913-1193	Peter W. Lewis Laboratory	N/A
Critical Commercial Assays		
PerfeCTa SYBR® Green SuperMix	Quanta Bio	Cat#95054-02K
SYBR Green PCR Master Mix	Thermo Fisher	Cat#4309155
REVERT Total Protein Stain	LI-COR Biosciences	Cat#926-11011
RevertAid First Strand cDNA Synthesis Kit	Thermo Fisher	Cat#K1621
Wizard® Genomic DNA Purification Kit	Promega	Cat#A1120
Dynabeads™ M-280 Sheep Anti Rabbit IgG	Thermo Fisher	Cat#11203D
QIAquick PCR Purification Kit	QIAGEN	Cat#28104
TruSeq DNA Nano	Illumina	Cat#20015964
Axygen™ Light Cycler 480 Compatible PCR Plates	Thermo Fisher	Cat#14-223-212
Promega MTase-Glo™	Promega	Cat#V7602
Deposited Data		

H3K9me1 and H3K9me3 ChIP-sequencing Data	This paper	GEO Accession Number: Available upon manuscript publication
RNA-sequencing Data	This paper	GEO Accession Number: Available upon manuscript publication
Experimental Models: Cell Lines		
H. sapiens: HCT116	ATCC	CCL-247
H. sapiens: HEK-293T	ATCC	CRL-3216
H. sapiens: HEK-293	ATCC	CRL-1573
H. sapiens: HepG2	ATCC	HB-8065
H. sapiens: MCF7	ATCC	HTB-22
H. sapiens: Panc1	ATCC	CRL-1469
M. musculus: Hepa-1c1c7	ATCC	CRL-2026
Experimental Models: Organisms/Strains		
M. musculus: C57BL/6J (9-weeks of age)	The Jackson Laboratory	JAX: 000664
M. musculus: C57BL/6J (2- and 18-months of age)	The National Institute on Aging Rodent Colony	N/A
Oligonucleotides		
5-Methylcytosine and 5-Hydroxymethylcytosine DNA	Zymo Research	Cat#D505
Stealth RNAi Sense Sequence: *H. sapiens* MAT2A: 5′AUCAAGGACAGCAUCACUGAUUUGG-3′	Thermo Fisher	Kera et al., 2013
Stealth RNAi Sense Sequence: Control: 5′-AGGAGGAUAUUACCAUGGACAAGAC-3′	Thermo Fisher	Kera et al., 2013
SUV39H1 RNAi: *H. sapiens*	Novus Biologicals	H00006839-R01-20nmol
SUV39H2 RNAi: *H. sapiens*	Novus Biologicals	H00079723-R01-20nmol
SETDB1 RNAi: *H. sapiens*	Novus Biologicals	H00009869-R01-20nmol
G9a/EHMT2 RNAi: *H. sapiens*	Novus Biologicals	H00010919-R02-20nmol

GLP/EHMT1 RNAi: *H sapiens*	Novus Biologicals	H00079813-R01-20nmol
RT-qPCR Primers	See Table S2	See Table S2
Software and Algorithms		
Bowtie2-2.1.0	Langmead and Salzberg, 2012	http://bowtie-bio.sourceforge.net/bowtie2/index.shtml
Samtools 1.5	Li et al., 2009	http://samtools.sourceforge.net/
MACS2-2.1.1.20160309	Zhang et al., 2008	http://liulab.dfci.harvard.edu/MACS/
Bedtools v2.25.0	Quinlan and Hall, 2010	https://bedtools.readthedocs.io/en/latest/
HOMER v4.9	Heinz et al., 2010	http://homer.ucsd.edu/homer/
GelAnalyzer 2010a	Lazar Software	http://gelanalyzer.com/index.html
MAVEN	Melamud et al., 2010; Clasquin et al., 2012	http://genomics-pubs.princeton.edu/mzroll/index.php
MAXQUANT	Cox et al., 2014	http://www.biochem.mpg.de/5111795/maxquant
Trimmomatic v0.39	Bolger et al., 2014	http://www.usadellab.org/cms/?page=trimmomatic
RSEM v1.2.4	Li et al., 2011	https://deweylab.github.io/RSEM/
GSEA 2	Tamayo et al., 2005 Mootha et al., 2003	http://software.broadinstitute.org/gsea/index.jsp
Skyline	MacLean et al., 2010	https://skyline.ms/project/home/software/Skyline/begin.view
Other		
Control *M. musculus* Diet	Envigo	TD.01084

Methionine Deficient *M. musculus* Diet	Envigo	TD.140119

1372 **Supplemental File Titles and Legends**

1373

1374 Document S1, Related to Figures 3 and S3. Primary Antibody and REVERT Total Protein Stain
1375 Western Blot Membranes.

1376

1377 (*A*) Cytoplasm anti-H3K9me1 (Figure 3E). (*B*) REVERT Total Protein Stain for cytoplasm anti-
1378 H3K9me1 (Figure 3E). (*C*) Cytoplasm anti-H3 (Figure 3E). (*D*) REVERT Total Protein Stain for
1379 cytoplasm anti-H3 (Figure 3E). (*E*) Cytoplasm anti-αTubulin (Figure 3E). (*F*) REVERT Total
1380 Protein Stain for cytoplasm anti-αTubulin (Figure 3E). (*G*) Nucleoplasm anti-αTubulin (Figure
1381 3E). (*H*) REVERT Total Protein Stain for nucleoplasm anti-αTubulin (Figure 3E). (*I*) Purified
1382 histone anti-H3K9me1 (Figure S3F). (*J*) REVERT Total Protein Stain for purified histone anti-
1383 H3K9me1 (Figure S3F).

1384

1385 Table S1, Related to Figures 1-3, 6-7, S1-S3, and S5. LC-MS/MS % Abundance Histone PTM
1386 Data.

1387

1388 Table S2, Related to Figures 2, 5, 7, S3, and S5. RT-qPCR Primers.

1389

1390 Table S3, Related to Figure 3. SILAC Cytoplasmic Proteins.

1391

1392

1393

Figure 1. Methionine Restriction Stimulates Dynamic Histone PTM Response

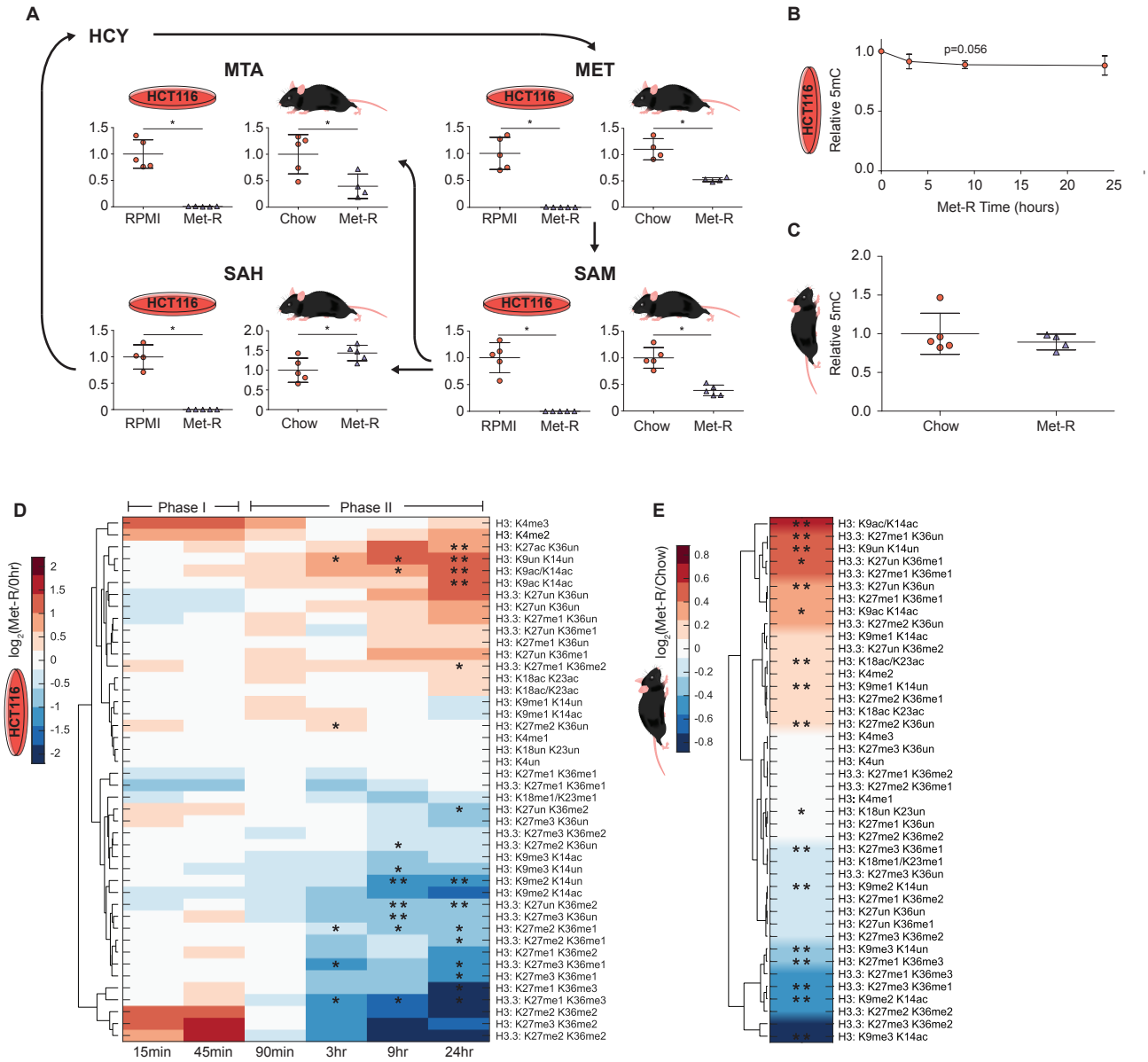

Figure 2. Decreased SAM Availability Drives Robust Histone Methylation Response

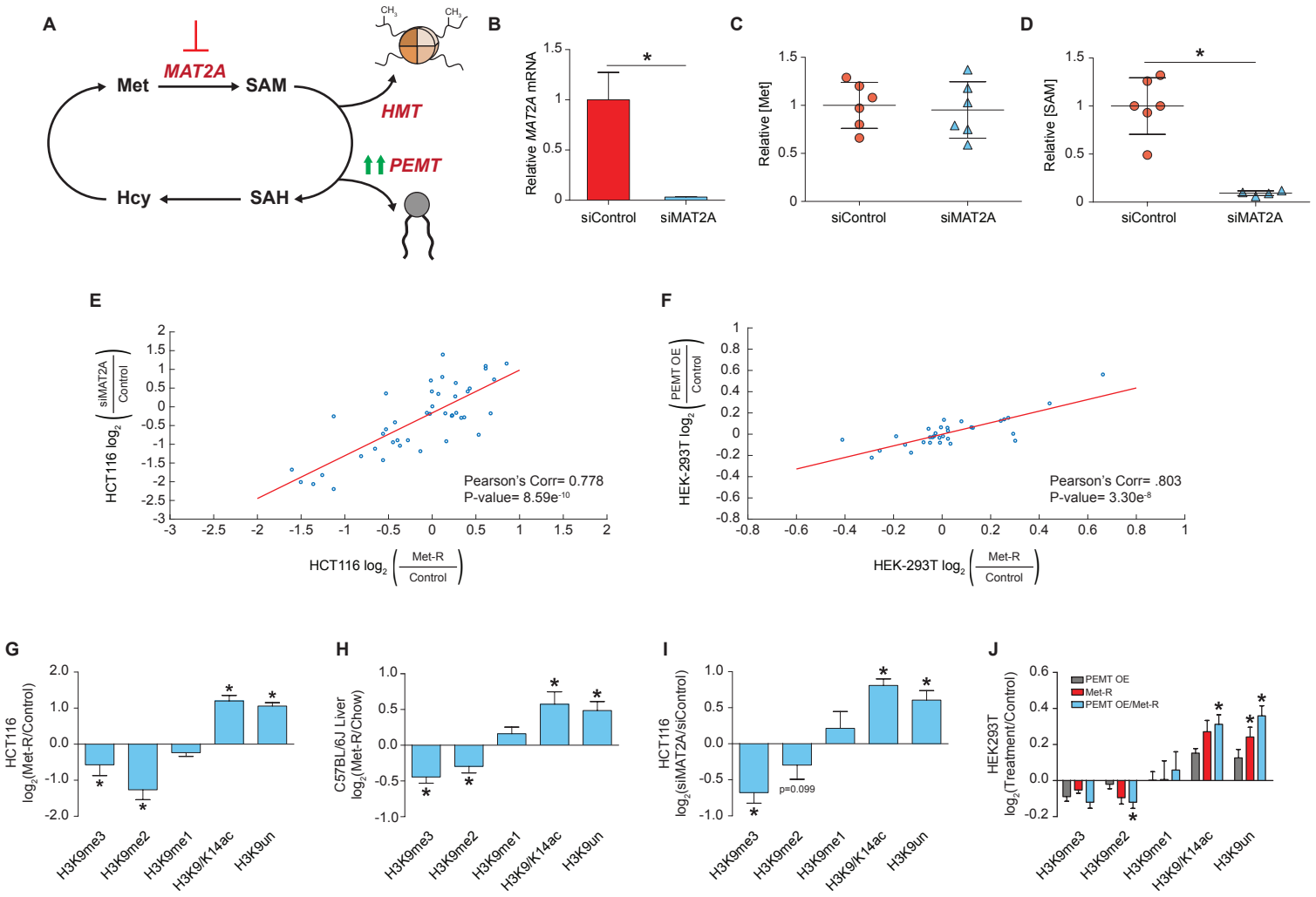

Figure 3. H3K9me1 Abundance under SAM Depletion is Driven by *de novo* Methylation

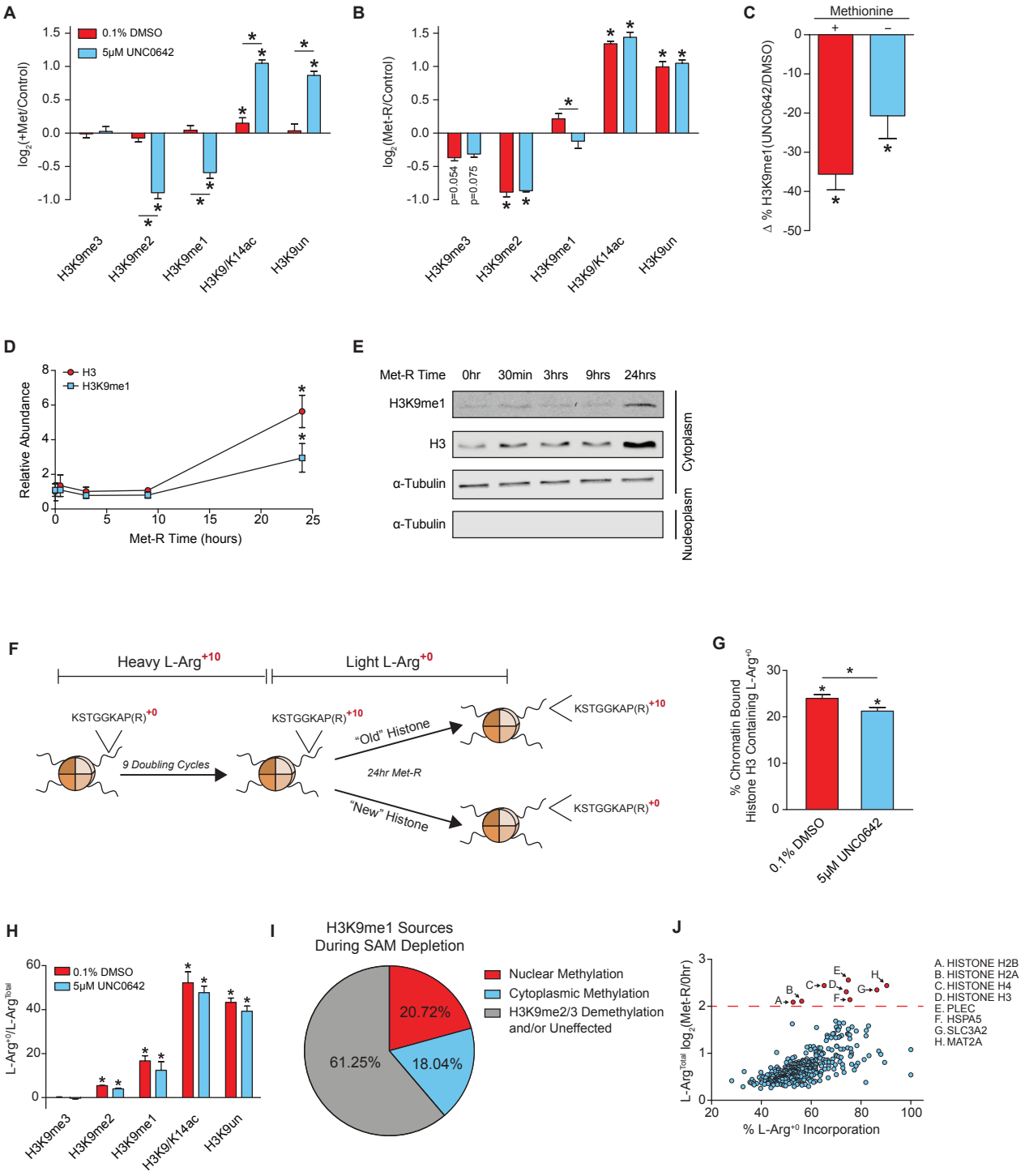

Figure 4. H3K9me1 is Redistributed Over Repetitive and Transposable Elements During SAM Depletion

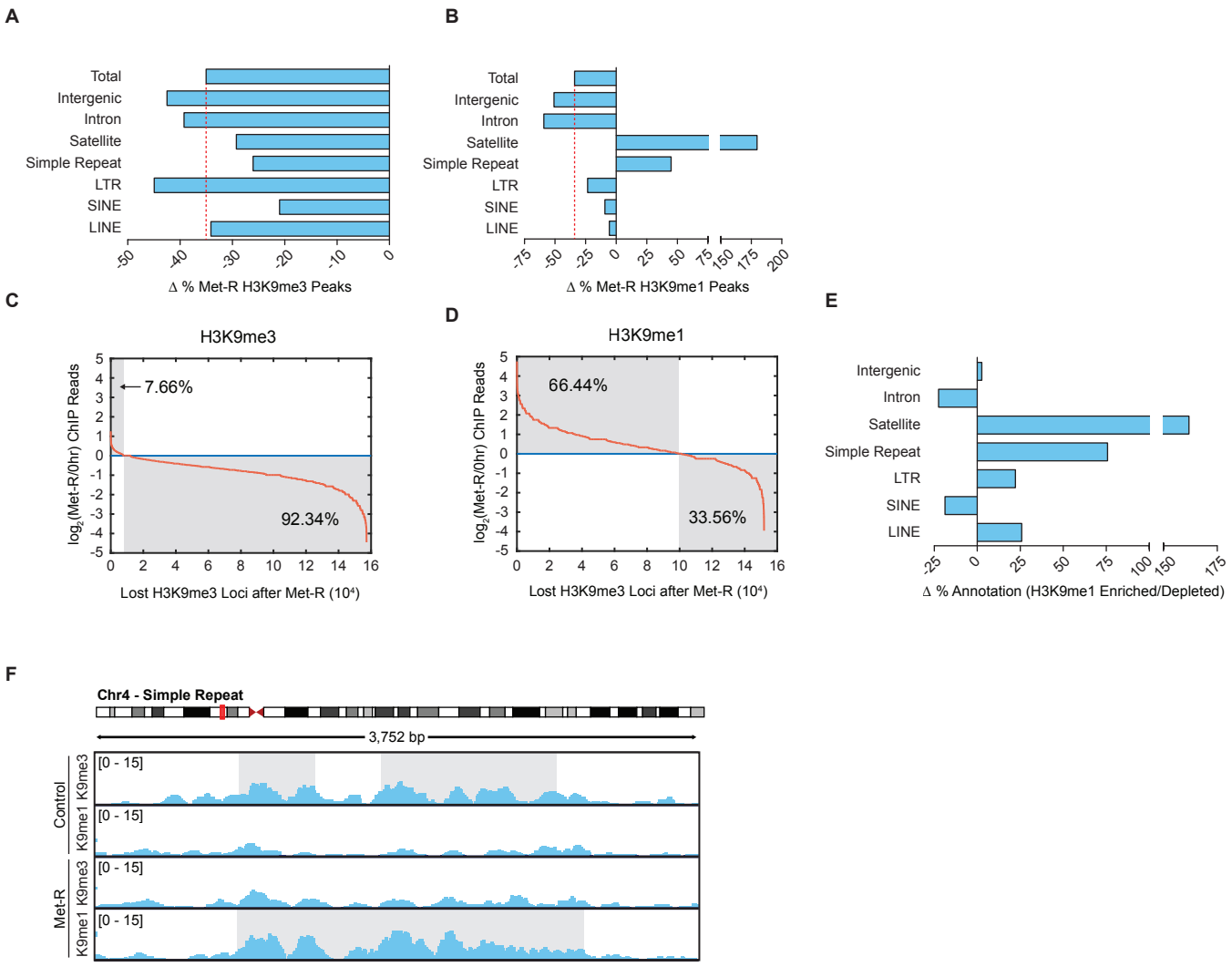

Figure 5. *De novo* H3K9 Mono-methylation Preserves Heterochromatin Stability

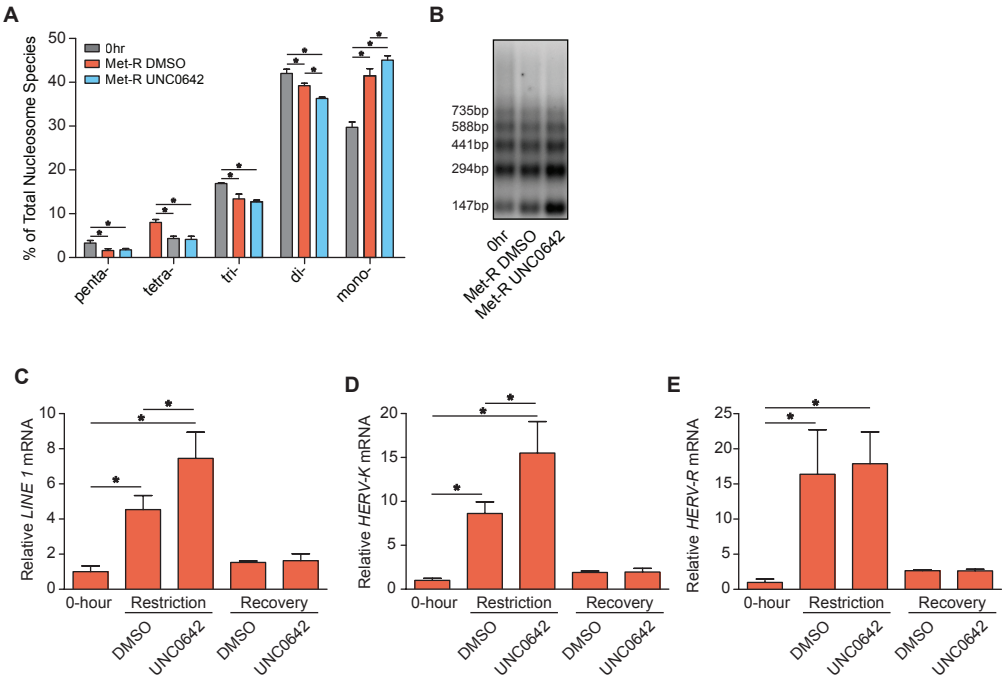

Figure 6. Adaptive H3K9 Mechanisms Support Epigenetic Persistence Upon Metabolic Recovery

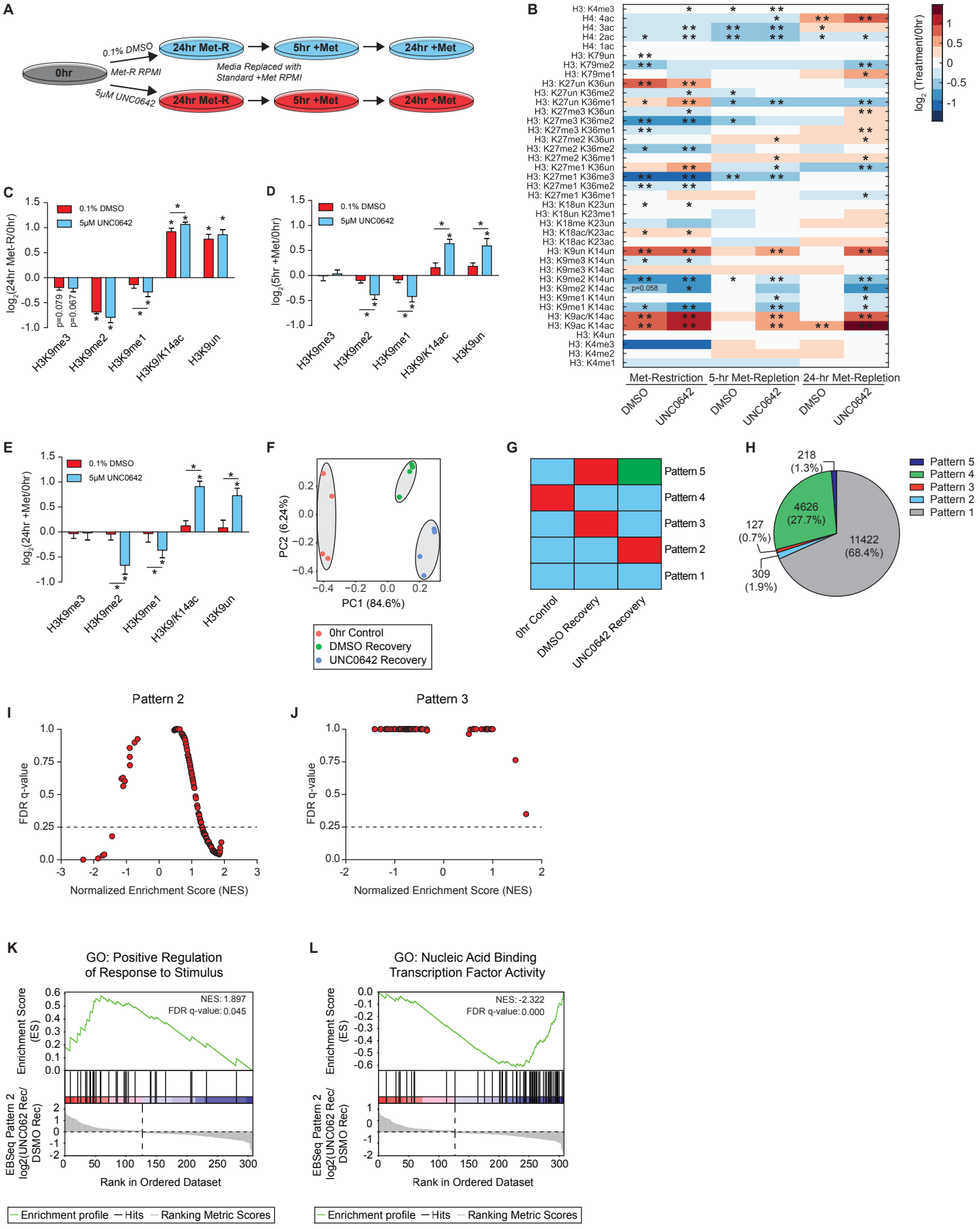

Figure 7. Adaptive and Persistent Epigenetic Responses to SAM Depletion are Robust *in vivo*, Independent of Age

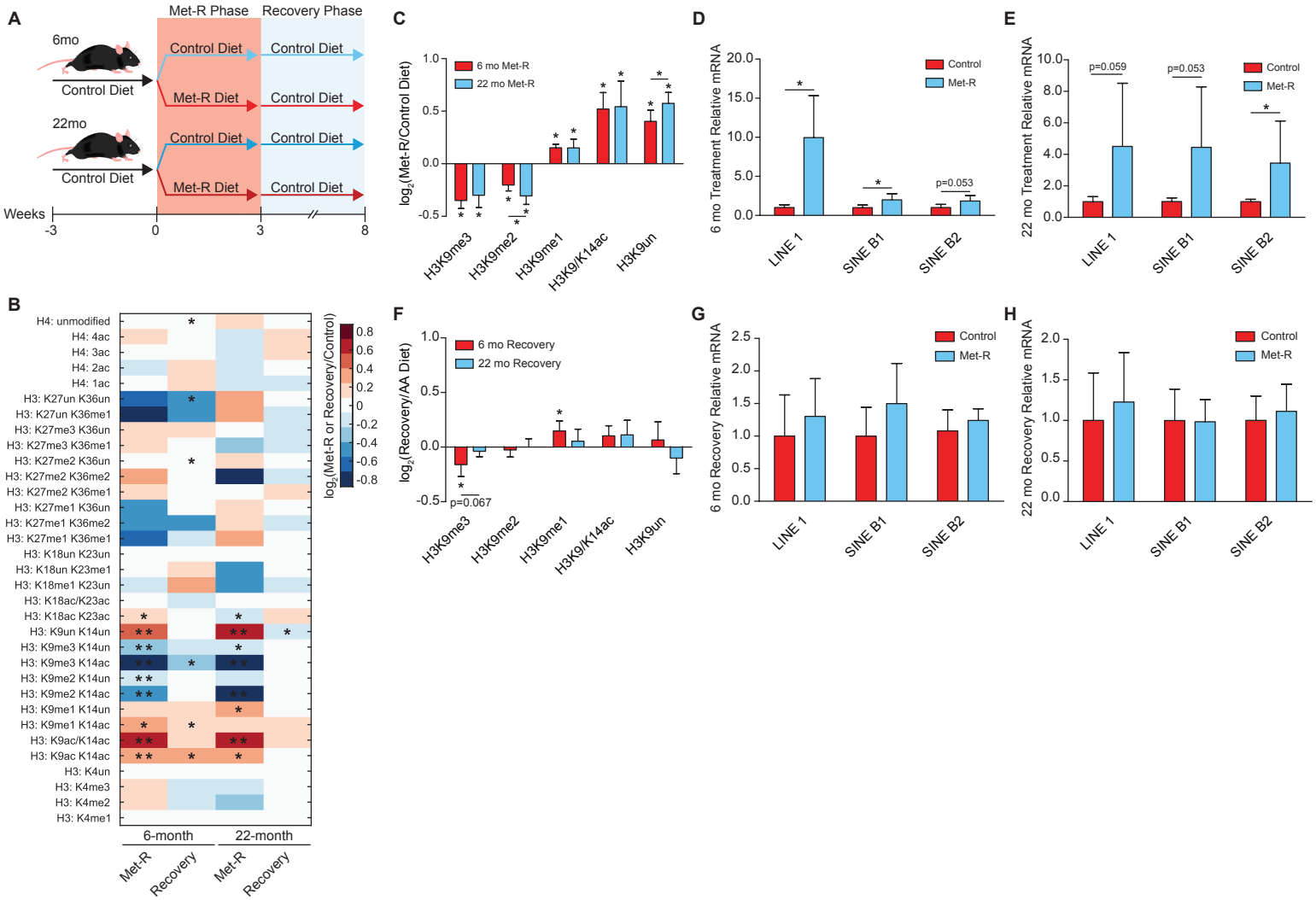

Figure S1. Related to Figure 1.

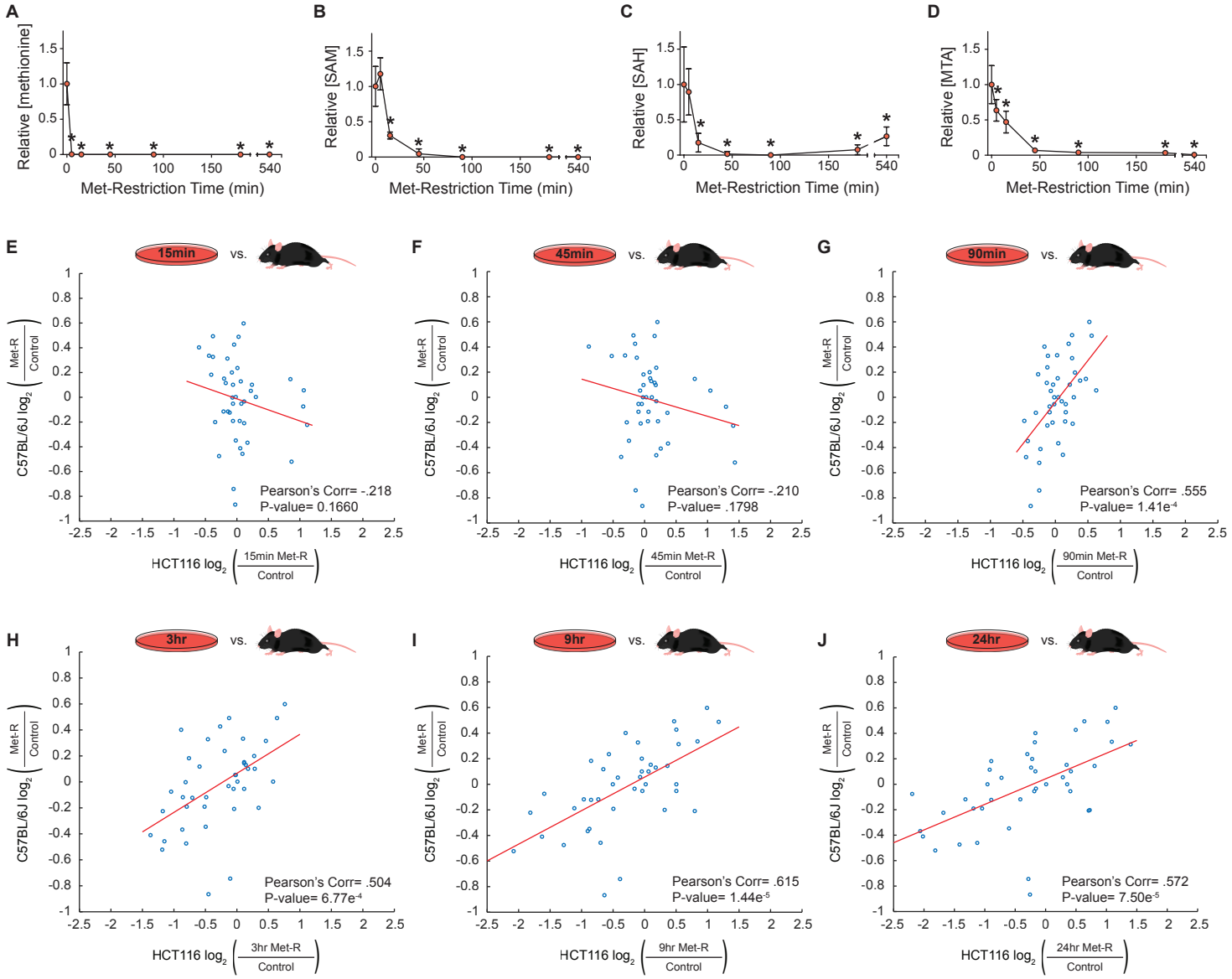

Figure S2. Related to Figure 2

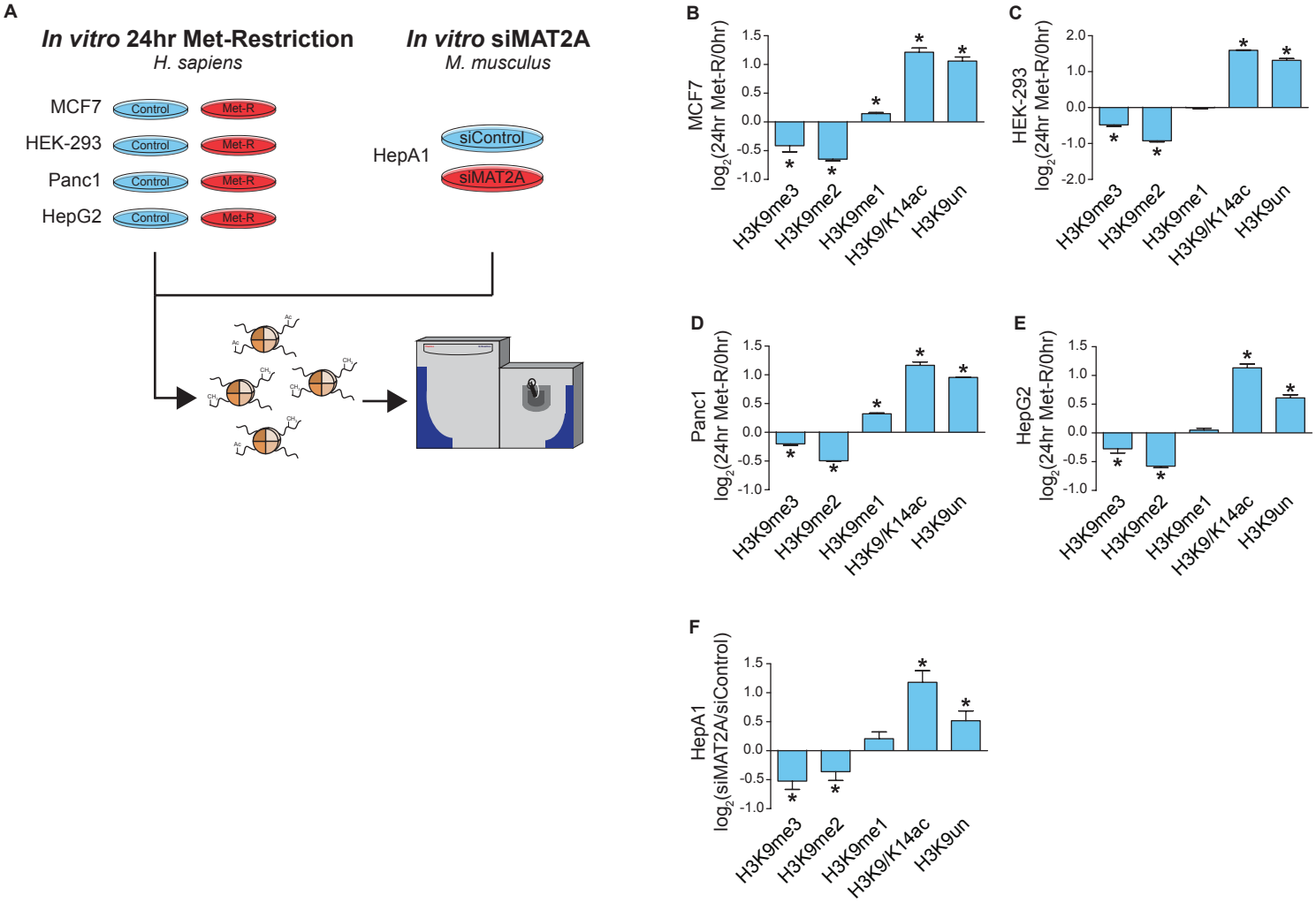

Figure S3. Related to Figure 3

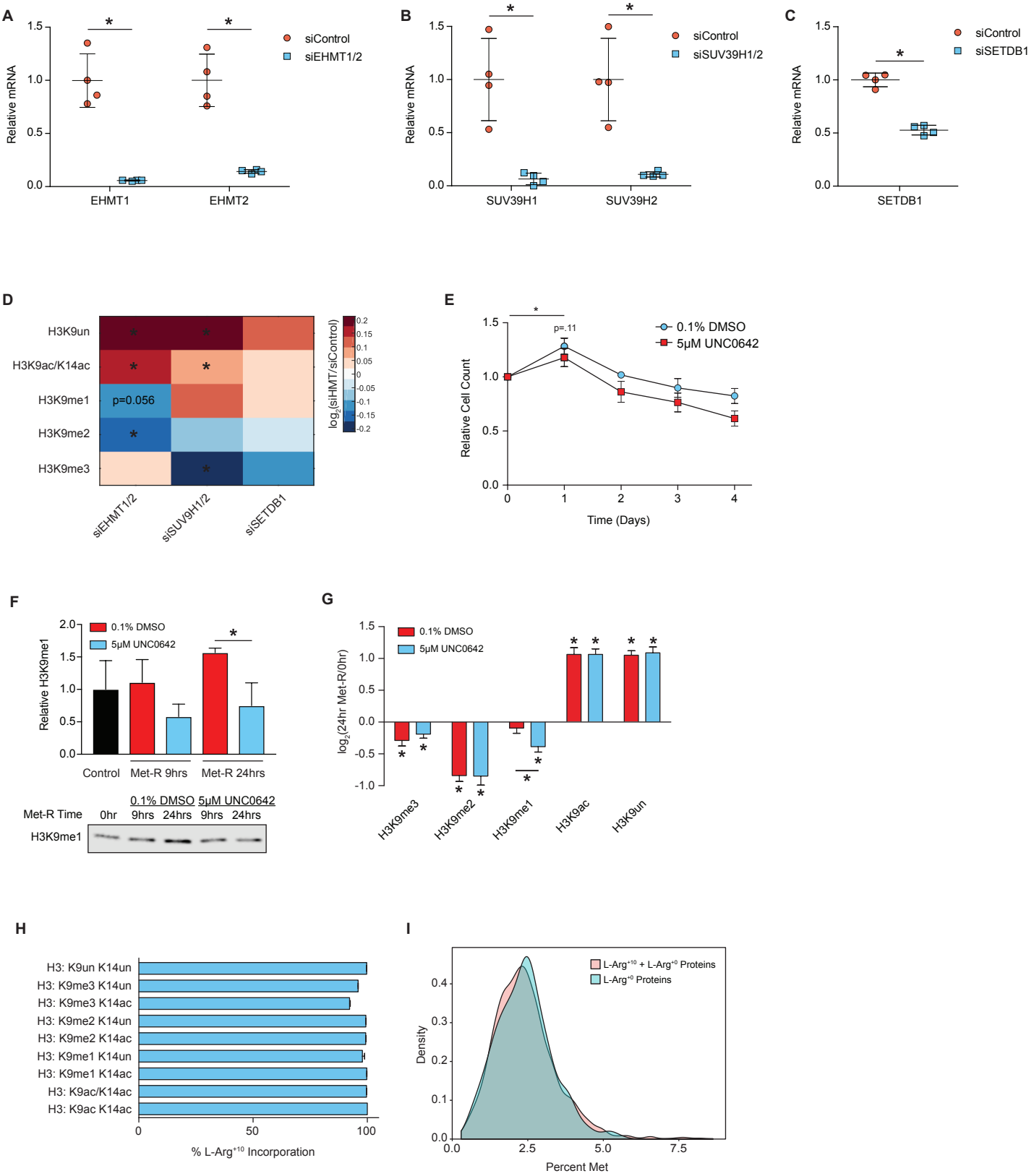

Figure S4. Related to Figure 6

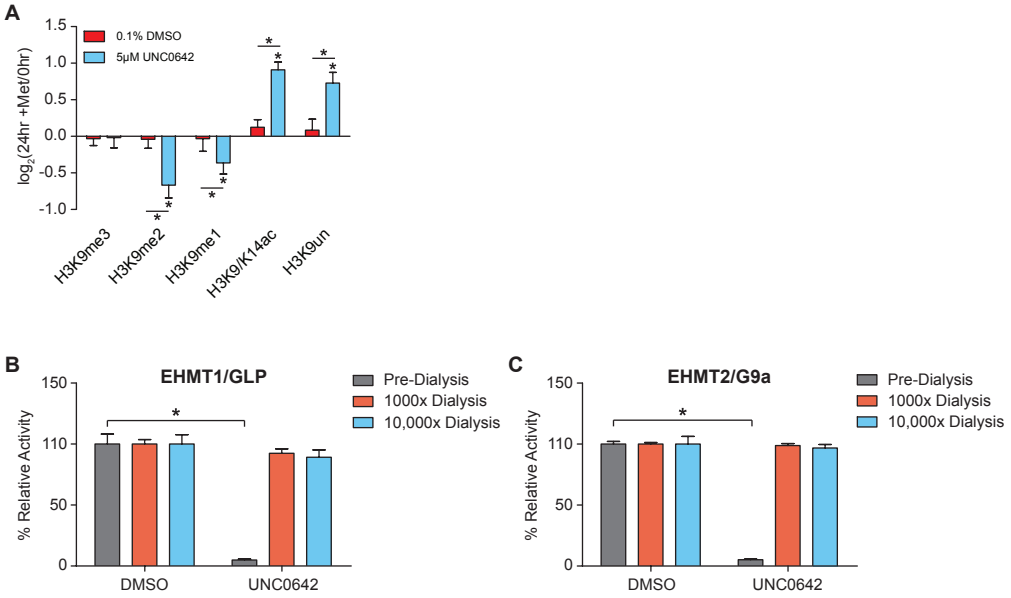

Figure S5. Related to Figure 6

A

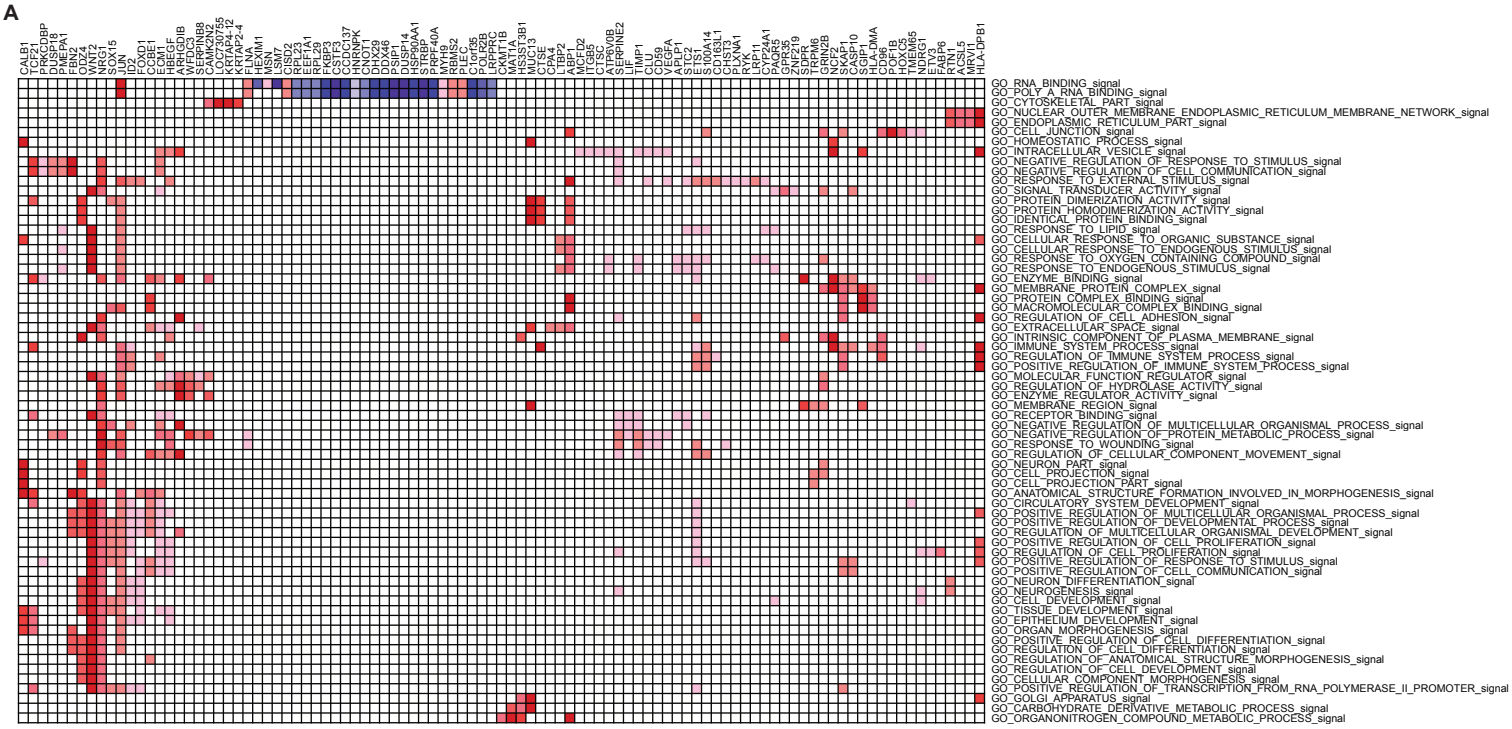

B

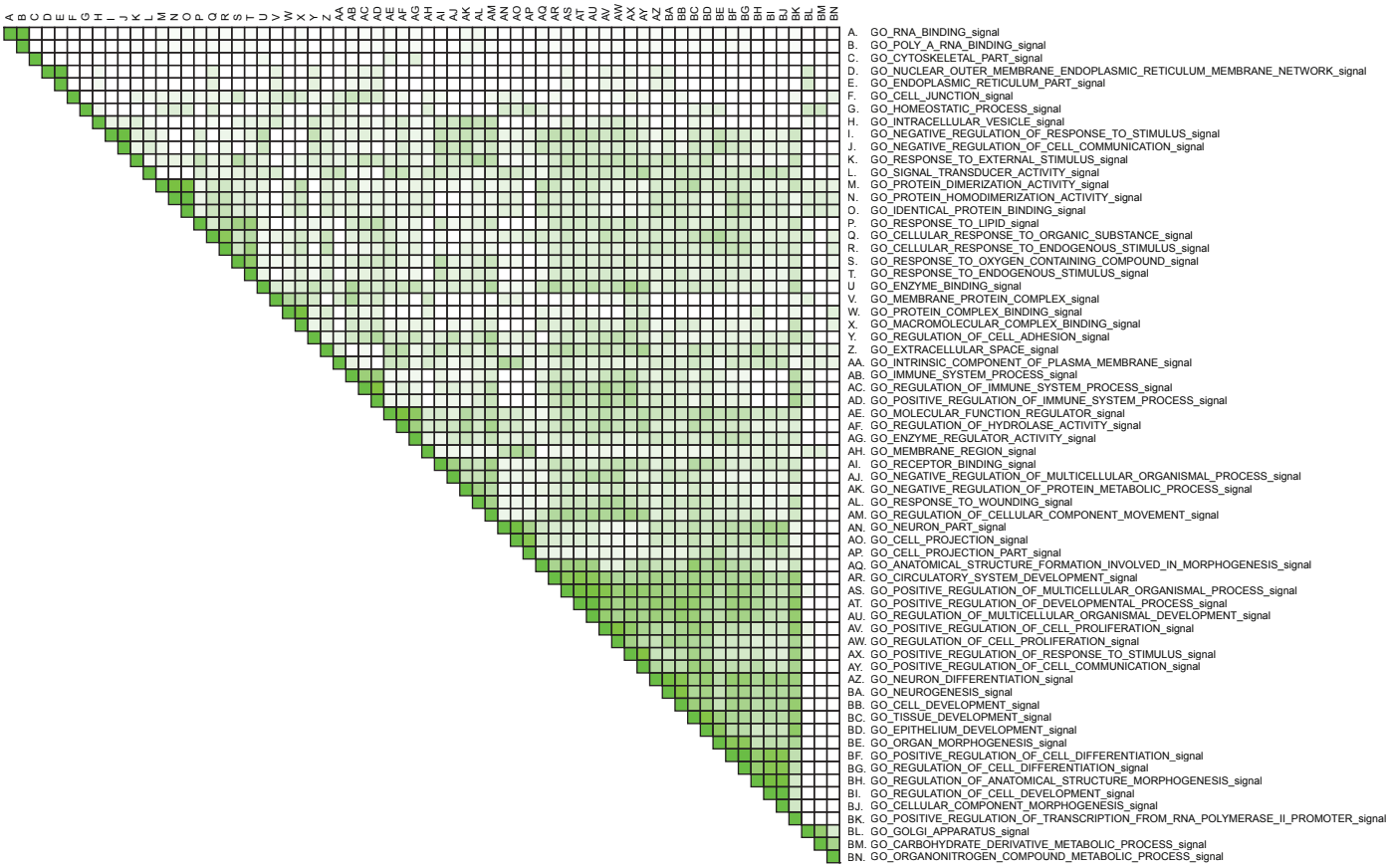

C

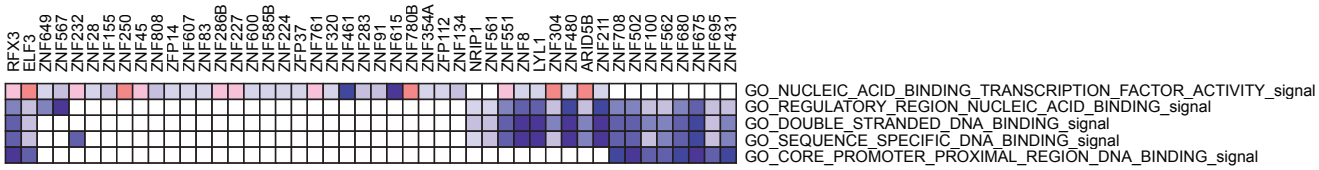
RFX3
ELF3
ZNF649
ZNF567
ZNF232
ZNF28
ZNF155
ZNF250
ZNF45
ZNF808
ZFP14
ZNF607
ZNF83
ZNF286B
ZNF227
ZNF600
ZNF585B
ZNF224
ZFP37
ZNF761
ZNF320
ZNF461
ZNF283
ZNF91
ZNF615
ZNF780B
ZNF354A
ZFP112
ZNF134
NRIP1
ZNF561
ZNF551
ZNF8
LYL1
ZNF304
ZNF480
ARID5B
ZNF211
ZNF708
ZNF502
ZNF100
ZNF562
ZNF680
ZNF675
ZNF695
ZNF431
GO_NUCLEIC_ACID_BINDING_TRANSCRIPTION_FACTOR_ACTIVITY_signal
GO_REGULATORY_REGION_NUCLEIC_ACID_BINDING_signal
GO_DOUBLE_STRANDED_DNA_BINDING_signal
GO_SEQUENCE_SPECIFIC_DNA_BINDING_signal
GO_CORE_PROMOTER_PROXIMAL_REGION_DNA_BINDING_signal

D

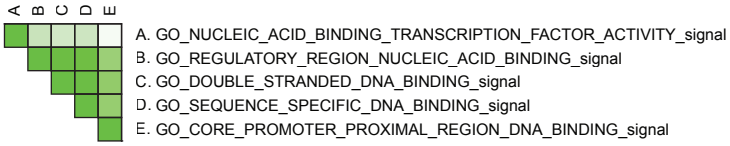
A
B
C
D
E
A. GO_NUCLEIC_ACID_BINDING_TRANSCRIPTION_FACTOR_ACTIVITY_signal
B. GO_REGULATORY_REGION_NUCLEIC_ACID_BINDING_signal
C. GO_DOUBLE_STRANDED_DNA_BINDING_signal
D. GO_SEQUENCE_SPECIFIC_DNA_BINDING_signal
E. GO_CORE_PROMOTER_PROXIMAL_REGION_DNA_BINDING_signal
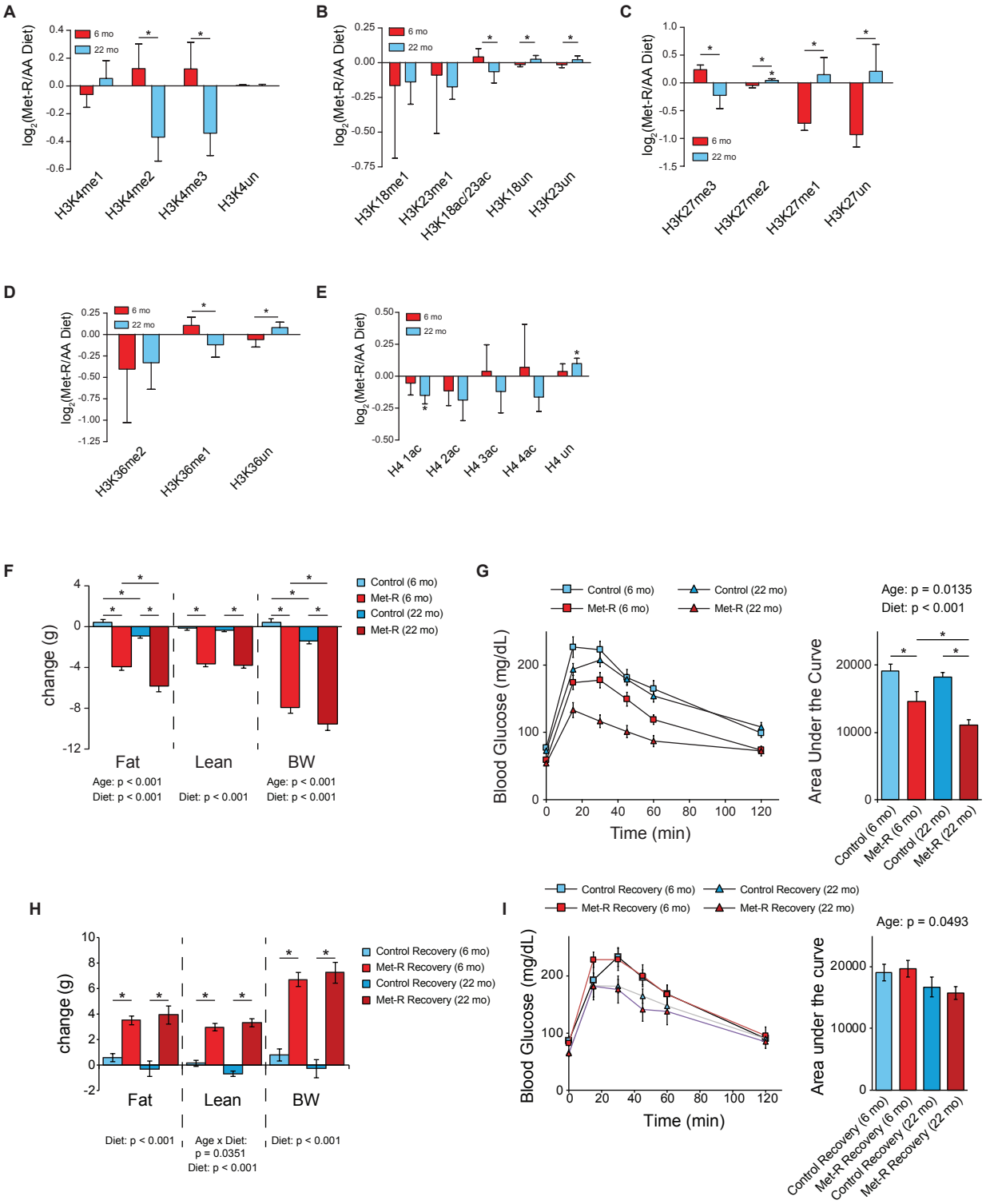
Figure S6. Related to Figure 7